



Simple physical-empirical model of the precipitation distribution based on a tropical sea surface temperature threshold and the effects of climate change

Yakelyn R. Jauregui¹ · Ken Takahashi¹

Received: 5 December 2016 / Accepted: 29 May 2017 / Published online: 14 June 2017
© Springer-Verlag Berlin Heidelberg 2017

Abstract The observed nonlinear relationship between tropical sea surface temperature (T_s) and precipitation (P) on climate timescales, by which a threshold (T_c) must be exceeded by T_s in order for deep convection to occur, is the basis of a physical-empirical model (PEM) that we fitted to observational data and CMIP5 climate model output and used to show that, with essentially only two constant parameters (T_c and the sensitivity a_1 of P to $T_s > T_c$), it provides a useful first-order description of the climatological and interannual variability of the large-scale distribution of tropical P given T_s , as well as of the biases of the Global Climate Models (GCMs). A substantial limitation is its underestimation of the peak P in the convergence zones, as the necessary processes associated with the atmospheric circulation are not considered. The pattern of the intermodel correlation between the mean $T_s - T_c$ for each GCM and the average P distribution is in agreement with the double ITCZ bias, featuring roughly zonally-symmetric off-equatorial maxima, rather than being regionally or hemispherically restricted. The inter-comparison of GCMs indicates a relationship between T_c with the near-equatorial low-level (850 hPa) tropospheric temperature, consistent with the interpretation that it is a measure of the convective inhibition (CIN). The underestimation of T_c is linked to the cold free tropospheric bias in the GCMs. However, the discrepancy among the observational datasets is a limitation for assessing the GCM biases from the PEM framework quantitatively. Under the RCP4.5 climate change scenario, T_c increases slightly more than the mean tropical T_s , implying a stabilizing trend consistent with the amplified

free tropospheric warming relative to the surface. However, since a_1 increases by 10–50%/°C with the surface warming, its effect dominates and results in generally positive precipitation change (ΔP) in the equatorial regions. In the equatorial eastern-central Pacific cold tongue, $\Delta(T_s - T_c)$ is positive, but the absolute $T_s - T_c$ remains small, which explains the double band pattern of ΔP along the equatorial flanks of the spuriously strong double ITCZs. When the GCM biases are corrected in the PEM, the positive ΔP in the southeast Pacific and Atlantic oceans is substantially reduced.

Keywords Double ITCZ · Critical temperature · Convective inhibition · Climate change

1 Introduction

There is a remarkable relationship between monthly-mean sea surface temperature (T_s) and precipitation (P) over the tropics, with major tropical rainfall confined within the 27 °C T_s contours (Bjerknes 1969; Manabe et al. 1974; Cornejo-Garrido and Stone 1977; Graham and Barnett 1987; Xie 2004). Although the ocean-atmosphere interaction is key to determining the joint distribution of T_s and P for the climatological mean (e.g. Takahashi and Battisti 2007a, b) and interannual variability, e.g. El Niño-Southern Oscillation, from a practical point of view it is useful to consider what the P distribution would be if we assumed the T_s as given.

Local thermodynamic control of P by T_s is associated with indices of parcel instability such as convective available potential energy (CAPE; Betts and Ridgway 1989; Williams and Renno 1993), convective inhibition (CIN; Mapes 1997) or a combination thereof (Raymond et al.

✉ Yakelyn R. Jauregui
yakki1529@gmail.com

¹ Instituto Geofísico del Perú, Lima, Peru

2003). According to Mapes (1997), the existence of CAPE is not a sufficient condition for deep convection. There are many areas where large-scale forcing creates CAPE, but deep convection only occurs in specific areas where mesoscale, and small-scale forcing can lift low-level parcel to their level of free convection. Therefore, deep convection could be controlled by boundary layer process that governs its initiation emphasizing the importance of overcoming the CIN (Mapes 1997).

Observations show a low sensitivity of monthly mean P to T_s for $T_s < 26^\circ\text{C}$ and a sharp increase of P above a critical T_s . This critical value may vary between 26 and 29 °C depending on the criteria and observational or modeling data (Gadgil et al. 1984; Graham and Barnett 1987; Fu et al. 1990; Waliser et al. 1993; Zhang 1993; Sud et al. 1999). This nonlinear threshold relation between P and T_s has been confirmed with different measures of deep convection such as cloudiness intensity (Gadgil et al. 1984), outgoing longwave radiation (OLR, Graham and Barnett 1987; Zhang 1993), the frequency of highly reflective clouds (HRC, Waliser et al. 1993), CAPE (Williams and Renno 1993; Fu et al. 1994; Bhat et al. 1996), and precipitation (Johnson and Xie 2010). It also has been used as the basis for simple parameterization schemes to estimate P given T_s (Kleeman 1991; Wang and Li 1993; Xie and Philander 1994; Back and Bretherton 2009b).

The existence of a critical T_s for deep convection has been linked at least implicitly with CIN, as it indicates the surface temperature required for a sufficiently reduced vertical stability of the tropical troposphere allowing the onset of large-scale moist convection (Lau and Shen 1988; Betts and Ridgway 1989; Johnson and Xie 2010; Johnson and Kosaka 2016). Since the tropospheric stability over the tropics is controlled by T_s in the convective regions due to the horizontal temperature gradients being weak in the free tropical troposphere (Neelin and Held 1987; Zeng and Neelin 1999; Sobel and Gildor 2003), this threshold is related directly to free troposphere temperature. This threshold is not absolute; it varies with the mean climate (Johnson and Xie 2010).

Interestingly, in regions where $T_s > 30\text{--}32^\circ\text{C}$, monthly mean P is low (Graham and Barnett 1987; Waliser and Graham 1993; Waliser et al. 1993; Zhang 1993; Meenu et al. 2012; Rajendran et al. 2012). This is explained by negative convective feedbacks on T_s , so that high T_s can only occur in non-convective conditions, involving processes such as evaporative cooling (Newell 1979), the combination of radiative balance and large-scale dynamics (Pierrehumbert 1995; Miller 1997; Larson et al. 1999), large-scale subsidence forced by local or remote deep convection (Lau et al. 1997) and detrained anvil cirrus effects on solar radiation (Graham and Barnett 1987; Ramanathan and Collins 1991; Waliser and Graham

1993; Chou and Neelin 1999). Clearly, high T_s should not be thought to “drive” low values of P in this case.

In addition to the thermodynamic control, the distribution of T_s affects the atmospheric boundary layer (ABL) dynamics. Firstly, horizontal T_s gradients are associated with thermally-induced horizontal pressure gradients in the ABL, which has a significant role in driving low-level convergence that promotes large-scale tropical convection, particularly in the eastern Pacific ITCZ where the meridional T_s gradients are large. Secondly, the distribution of T_s also influences the surface winds due to its influence on mixing in the ABL, so that wind speed tends to be large where T_s is high. Back and Bretherton (2009b) estimated that local control is important for deep convection over the western Pacific ocean while T_s gradients are important for the eastern Pacific ITCZ, where the meridional T_s gradients are large.

While a given T_s distribution promotes P , atmospheric positive feedback mechanisms can further enhance P . One such mechanism is linked to the circulation facilitated by the latent heat release, which in turn can increase the local low-level moisture influx (Waliser and Somerville 1994; Gu and Zhang 2001).

Under global warming, the change in the P distribution (ΔP) is strongly associated with the changes in T_s (Xie et al. 2010; Chadwick et al. 2013; Chung et al. 2014; Ma and Xie 2013; Huang et al. 2013) although changes in the T_s gradients also play a significant role (Xie et al. 2010; Kent et al. 2015; Chung et al. 2014; Power et al. 2013; Cai et al. 2014; Grose et al. 2014).

Currently, there are two conceptual frameworks for describing ΔP . One is the “wet-get-wetter” theory, by which the increased water vapor content in a warming troposphere with constant relative humidity enhances the existing contrasts between wet and dry regions (Neelin et al. 2003; Held and Soden 2006; Chou et al. 2009). This framework is predictive in that it needs only the current P distribution and a measure of the overall warming trend to yield the change in the P distribution; however, the correlation between the current P and ΔP patterns is low (Chadwick et al. 2013). This theory can be complemented by considering the missing terms such changes in the circulation (Bony et al. 2013; Chadwick et al. 2013), but the theory then becomes diagnostic rather than predictive.

The other is the “warmer-gets-wetter” theory, which predicts increased rainfall where the T_s exceeds the mean surface warming in the tropics, i.e. focusing on the tropospheric stability or CIN as the limiting factor for deep convection (Vecchi and Soden 2007b; Xie et al. 2010; Johnson and Xie 2010; Sobel and Camargo 2011), taking into account the non-local effect of the surface warming in the convective regions on stability.

On the other hand, global climate models (GCMs) have common biases that affect the future projections, and the ΔT_s pattern is arguably the largest source of uncertainty in the changes of P over the tropical oceans and circulation (Huang et al. 2013; Ma and Xie 2013; Huang 2014). However, the role of ΔT_s is weaker for land precipitation (Chadwick 2016). Understanding how these biases affect the climate change projections is essential to reduce structural uncertainty.

In this study, we explore the usefulness of a simple physical-empirical model (PEM) to describe and offer insights on the distribution of the tropical P as a response to T_s . The PEM is essentially a crude parameterization scheme that allows us to estimate the large-scale monthly mean tropical P given the local value of T_s and is conceptually based on the idea of CIN being a limiting factor for deep tropical convection. The value of this approach is that it is not only simple conceptually but that it depends on only two constant parameters (four in the complete version) for a given basic climate (present day or future), thus providing metrics for describing the differences among climate states and GCMs (similar to Bellucci et al. 2010).

In the following section, we describe the data used. Next, we describe the formulation of the two versions of the PEM. After that, we fit the PEM to the observational data and present its validation, as well as sensitivities to data sources. We then repeat with the GCM data, which includes coupled and atmosphere-only experiments. We show that the critical temperature for convection varies among GCMs and experiments with the free troposphere temperature, and that the PEMs describe the climate change effect on the pattern of P . We also apply a simple bias correction to the PEM to assess the effects of the GCM biases on the projections.

2 Data

2.1 Observational datasets

Our observational analyses are based on monthly mean gridded products. To test the sensitivity of our results to different observational products, we select a set for each variable. The original grid size and availability period are indicated in Table 1. If necessary, the datasets were interpolated to a $1^\circ \times 1^\circ$ grid.

For precipitation (P), we use primarily the Global Precipitation Climatology Project (GPCP) version 2.2 (Huffman et al. 1997; Adler et al. 2003) product. For comparison, we also consider the Climate Prediction Center (CPC) Merged Analysis of Precipitation (CMAP) (Xie and Arkin 1997) and Tropical Rainfall Measuring Mission (TRMM)

Table 1 Observational datasets

Variable	Product	Grid spacing	Period
P	GPCP	$2.5^\circ \times 2.5^\circ$	1979–2015
	CMAP	$2.5^\circ \times 2.5^\circ$	1979–2015
	TRMM	$0.25^\circ \times 0.25^\circ$	1998–2015
	AMIP-SST	$1^\circ \times 1^\circ$	1979–2008
T_s	ERSST	$2.5^\circ \times 2.5^\circ$	1979–2015
	OISST	$1^\circ \times 1^\circ$	1981–2015
	HADISST	$2.5^\circ \times 2.5^\circ$	1979–2015
	Reanalysis 2	$2.5^\circ \times 2.5^\circ$	1979–2008
T_a	ERA-Interim	$1^\circ \times 1^\circ$	1979–2008
	AIRS	$1^\circ \times 1^\circ$	2002–2016

3B43 precipitation product (Kummerow 2000; Huffman and Bolvin 2011).

For sea surface temperature (T_s), we use the monthly mean surface temperature or skin temperature (i.e., sea surface temperature over the oceans) output from the *Atmospheric Model Intercomparison Project* (AMIP) experiments in the CMIP5 database (see next section for more details). We use an average across the models because although every modeling center is supposed to follow the same procedure to prepare the T_s fields (Hurrell et al. 2008), in practice the latter are slightly different (up to 0.02° of difference in the tropical mean from the multimodel annual average; not shown). The difference in the spatial distribution of the mean T_s is very evident for the GISS-E2-R and IPSL-CM5A-MR models, with differences of up to 0.5° from the multimodel mean (not shown). We refer to this dataset as AMIP-SST. For comparison, we also use the NOAA Optimum Interpolation SST version 2 (OISST V2) (Reynolds et al. 2002), NOAA Extended Reconstructed SST version 4 (ERSST V4; Reynolds and Smith 1994), and the global Hadley Center Global SST (HadISST) analysis (Rayner et al. 2003) products. Our final results are not sensitive to the choice of any dataset.

For atmospheric temperature (T_a), we use the NCEP/DOE Reanalysis 2 (Kanamitsu et al. 2002), the ERA Interim reanalysis (Dee et al. 2011) and the monthly mean tropospheric air temperature data from the Aqua Atmospheric Infrared Sounder (AIRS) version 6 level-3 product, which includes data from the Advanced Microwave Sounder Unit (AMSU) and Humidity Sounder for Brazil (HSB) (Susskind et al. 2011; Tian et al. 2013).

2.2 Global climate models

We examine 26 global climate models (GCMs) from the *historical* experiment (HIS) that extend from mid-19th century to near-present with observational radiative forcing, and the intermediate greenhouse gas emission scenario

Representative Concentration Pathway 4.5 (RCP4.5) simulations from the World Climate Research Programme (WCRP) Coupled Model Intercomparison Project Phase 5 (CMIP5) multimodel ensemble (Taylor et al. 2012), as well as 11 from the AMIP experiments also in the CMIP5 database, which consists of running the atmospheric component of the GCMs with sea surface temperature prescribed to common observed values (Gates 1992). Here, we only use the first member from each ensemble for each model in the CMIP5 dataset (we tested using all members for all the IPSL models and GISS-E2-R and found no substantial effect).

In this study, we use 30 years of monthly mean surface temperature or skin temperature (T_s , i.e., sea surface temperature over the ocean), precipitation (P), and atmospheric temperature (T_a). We use only 22 out of 26 models from the HIS and RCP4.5 experiments of T_a and the 11 models from AMIP (Table 2) that were available. We analyze 1971–2000, 1979–2008, and 2061–2090 periods for the HIS, AMIP, and RCP4.5 experiments, respectively. Since models have different spatial resolutions, we bilinearly interpolated the data to a common $1^\circ \times 1^\circ$ grid before the analysis.

3 Formulation of the physical–empirical model (PEM)

Our primary interest is to use a simple model with two parameters, the threshold in sea surface temperature for deep convection (T_c) and the rate (a_1) with which P increases with T_s above T_c , that can explain many features of the tropical precipitation distribution and the effect of climate change.

However, a nonlinear optimization that minimizes the RMS error using a simpler estimation of monthly rainfall as a linear function of T_s above a threshold, results in low T_c and a_1 that are not representative of T_s/P dispersion. Therefore, we include two more parameters, the temperature T_{p90} above which P decreases with T_s , and the rate (a_2) with which P decreases with T_s above T_{p90} . The consideration of these new parameters prevents the overestimation of P at very high T_s , where in fact monthly rainfall seems to be suppressed by large-scale conditions (Zhang 1993; Waliser and Graham 1993; Waliser et al. 1993; Lau et al. 1997; Sud et al. 1999). Besides, they improve the estimation of T_c and a_1 reducing the RMS error relative to the simpler version. We call PEM to the version with these four parameters and PEM2 to the version that only considers the same T_c and a_1 as PEM but does not constrain P above T_{p90} (effectively considering $T_{p90} \rightarrow \infty$). These four parameters do not vary in space or time for a given climate.

The spatial domain spans from 20°S to 20°N, which contains all the tropical convergence zones but not the subtropical ones, which are not as tightly tied to sea surface temperature (Fig. 1a). It is important to mention that PEM does not consider the horizontal gradients in T_s , so the associated forced convergence does not affect our estimation of P .

The PEM is formulated as

$$P = \begin{cases} 0; & T_s < T_c \\ a_1(T_s - T_c); & T_c \leq T_s \leq T_{p90} \\ a_2(T_s - T_{p90}) + a_1(T_{p90} - T_c); & T_{p90} < T_s \leq T_x \\ 0; & T_x < T_s \end{cases} \quad (1)$$

where, $T_x \equiv a_1/a_2(T_c - T_{p90}) + T_{p90}$.

To fit the model, we bin the monthly P data according to the local T_s using 0.1°C bins. The value of T_{p90} corresponds to the center of the T_s bin for which the 90-percentile of P is the largest (the results are not sensitive to using the 90, 95 or 99 percentiles). We searched for the value of T_c that resulted in the best fit by varying T_c on 0.01°C increments and performing the fit for each. Thus, for each T_c , we assumed that $P = 0$ for $T_s \leq T_c$ and a linear regression was used to determine a_1 . Then we fixed the value of P at T_{p90} estimated from these parameters and use linear regression to find a_2 and T_x . Finally, we calculate the RMS error between the estimated and the actual P . The set of parameters selected are those that minimize the RMS error. For $T_s > T_x$, P is set to zero (Fig. 1e).

To test the statistical significance of the fit, we use the bootstrap analysis (Efron and Tibshirani 1993), and we estimate the 95% confidence intervals for each parameter. For each model and observational dataset, 5000 bootstrap samples were generated by randomly sampling, with replacement, 10% of each original dataset (approximately 400,000 data points). The confidence intervals do not change noticeably if the sample lengths are varied from 10 to 50%.

The time-varying P fields reconstructed using the PEM are denoted as $\text{PEM}(T_s; T_c, T_{p90}, a_1, a_2)$. For the RCP4.5 scenario, the values are denoted with a prime (i.e. $T'_s, T'_{p90}, T'_c, a'_1, a'_2$) and the changes relative to the present are denoted with a delta (e.g. $\Delta T_c = T'_c - T_c$). The climate change effect on P from the GCMs is then estimated with the PEM as a difference of the future esceenario minus the present.

Keeping in mind that T_c and a_1 are the same for PEM and PEM2, we compare the estimation the P distribution using PEM and PEM2 for different observational datasets and GCMs for the historical simulation. However, we only use the PEM2 to correct the effect of the systematic biases (e.g., the double ITCZ and the cold tongue

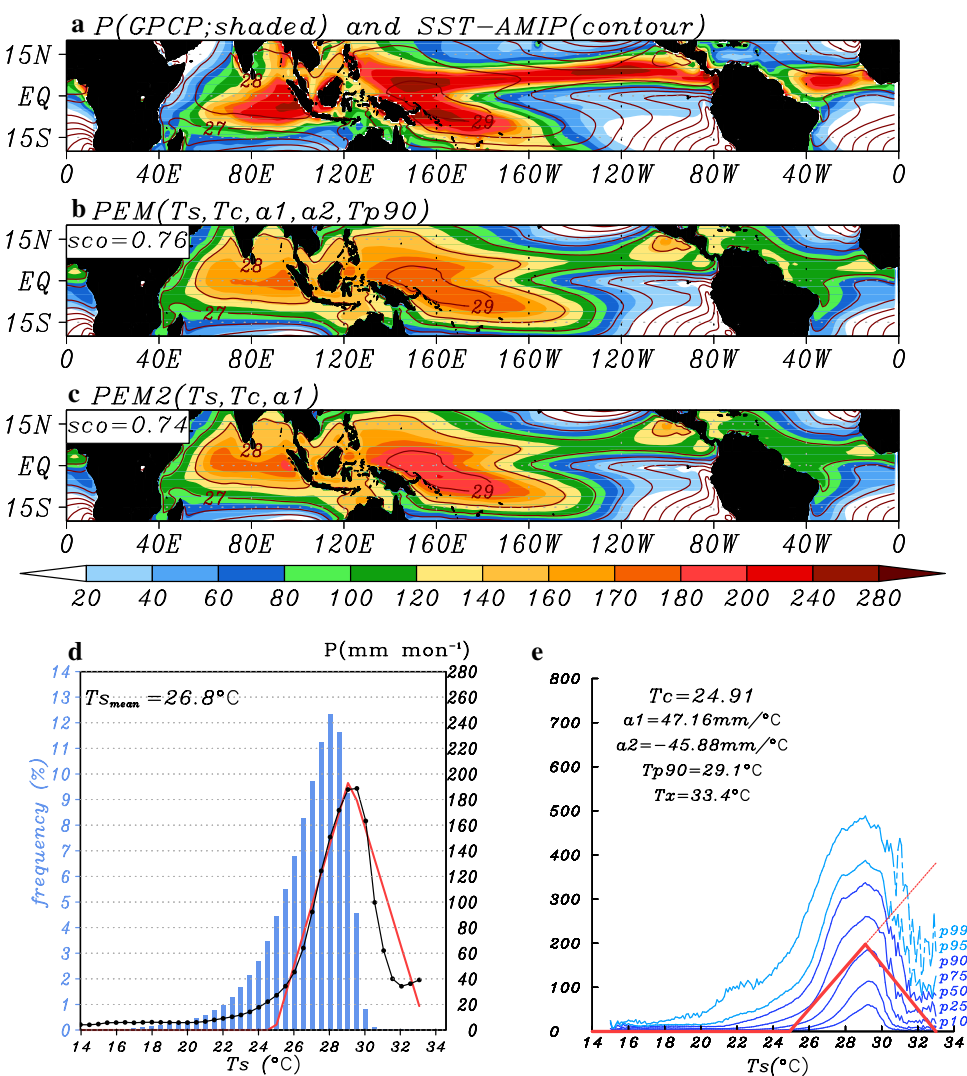
Table 2 PEM parameters fitted to the three GCM experiments. GCMs for which T_a was not available are indicated with (x)

#	Model name	HIS						RCP4.5	
		T_c	T_{p90}	a_1	a_2	T'_c	T'_{p90}	a'_1	a'_2
a	ACCESS1-0 (x)	25.05	28.90	79.21	-71.29	26.92	30.60	89.60	-87.44
b	ACCESS1-3 (x)	25.56	29.30	83.84	-90.83	27.55	30.90	98.97	-82.90
c	bcc-csm1-1-m	25.16	29.60	54.03	-57.13	26.44	31.00	55.54	-80.36
d	bcc-csm1-1	24.50	28.90	53.31	-93.40	25.94	29.90	58.79	-70.02
e	CanESM2	25.05	29.40	65.49	-69.05	27.00	31.00	72.31	-71.06
f	CCSM4	24.87	31.10	52.96	-136.25	26.65	29.70	70.51	22.03
g	CESM1-BGC	24.93	31.00	53.35	-137.32	26.68	29.70	71.37	19.76
h	CESM1-CAM5	23.36	30.10	43.30	-147.82	25.85	29.70	63.07	-1.21
i	GFDL-CM3	24.23	27.90	69.16	-35.06	26.57	30.00	78.09	-30.89
j	GFDL-ESM2G	24.06	28.50	59.34	-44.45	25.36	29.40	65.32	-35.95
k	GFDL-ESM2M	24.44	29.20	61.07	-72.45	25.87	29.90	68.66	-42.06
l	GISS-E2-H-CC	24.76	28.60	59.34	-34.29	25.86	30.90	56.42	-171.91
m	GISS-E2-H	24.66	28.40	59.40	-29.74	25.70	30.80	54.46	-160.41
n	GISS-E2-R-CC	24.85	28.30	62.57	-18.27	26.09	29.40	67.38	-16.88
o	GISS-E2-R	24.88	28.40	62.88	-26.07	26.12	29.40	68.66	-19.50
p	HadGEM2-AO	25.31	29.30	81.26	-65.51	27.26	30.80	91.61	-57.60
q	HadGEM2-CC (x)	24.68	28.60	79.38	-60.27	26.56	30.10	91.03	-60.76
r	HadGEM2-ES	24.95	28.90	81.59	-61.48	26.94	30.70	89.13	-62.70
s	IPSL-CM5A-LR	24.62	27.90	64.97	15.37	26.89	30.00	79.49	-9.74
t	IPSL-CM5A-MR	25.41	28.80	67.00	15.31	27.48	30.60	73.65	15.31
u	IPSL-CM5B-LR	25.07	29.40	60.83	-116.35	26.67	29.60	74.32	13.04
v	MPI-ESM-LR	24.71	28.40	70.60	-22.81	26.30	29.90	78.41	-33.75
w	MPI-ESM-MR	24.45	30.80	57.82	-124.20	26.56	30.40	79.51	-63.01
x	MRI-CGCM3	25.26	28.90	77.15	-81.79	26.46	30.50	77.57	-166.17
y	NorESM1-ME	23.76	29.80	53.11	-133.37	24.96	30.70	55.32	-186.70
z	NorESM1-M (x)	23.88	30.00	52.53	-134.04	25.41	29.10	65.33	10.17
	Average	24.71	29.17	64.06	-70.48	26.39	30.18	72.87	-55.03
#	Model name	AMIP							
		T_c	T_{p90}			a_1	a_2		
c	bcc-csm1-1-m	25.07				57.30			-172.34
d	bcc-csm1-1	25.44				63.58			-161.92

Table 2 (continued)

#	Model name	AMIP			
		T_c	T_{p90}	a_1	a_2
i	GFDL-CM3	24.97	28.50	68.38	-26.87
o	GISS-E2-R	23.95	29.30	50.55	-129.24
p	HadGEM2-A	25.35	29.60	72.51	-82.12
s	IPSL-CM5A-LR	24.77	30.20	50.39	-163.08
t	IPSL-CM5A-MR	24.79	30.60	49.98	-177.30
u	IPSL-CM5B-LR	25.43	30.20	65.73	-199.11
v	MPI-ESM-LR	25.45	30.20	74.13	-155.11
w	MPI-ESM-MR	25.42	30.20	74.31	-131.16
x	MRI-CGCM3	25.61	29.50	76.74	-103.64
	Average	25.11	29.86	63.96	-136.54

Fig. 1 **a** Time-averaged 1979–2008 of precipitation (shaded; mm month⁻¹; data from GPCP) and sea surface temperature (contours; °C; AMIP-SST), **b** similar to **a**, but time-averaged precipitation estimated by PEM, **c** similar to **a**, but time-averaged precipitation estimated by PEM2, **d** T_s histogram binned by 0.5 °C, rainfall mean for each T_s bin (black line for GPCP, red line for PEM) **e** scatter plot of monthly T_s against observed precipitation (blue) and against P estimated by PEM (thick red line) and PEM2 (thin dashed red line); blue (light blue) lines correspond to 10, 25, 50, 75 and 90 (95 and 99) rainfall percentiles for each 0.1 T_s binned



bias) in the models on the climate change projections of P by combining the observed present-day estimates of T_s , T_c and a_1 and the future changes from the GCMs (Δ for T_s and T_c , and the fractional change in a_1). By doing so, we avoid the consideration of changes in a_2 and T_{p90} that would be difficult to interpret.

4 Application of the PEM to observational data

Our reference datasets are AMIP-SST and GPCP (1979–2008), since the former eases the comparison to the AMIP model experiments, while the latter is a well-known and studied dataset (although we later show these two particular datasets to be different from the rest). The PEM fitted to these datasets produces a spatial distribution of mean P (Fig. 1b) that is similar to the observed (Fig. 1a), with a spatial correlation coefficient of 0.76 (0.74 for PEM2; Table 3), higher than the value of 0.67 obtained by Back and Bretherton (2009b) with a simpler model. P is strongly tied to T_s , although a purely linear model of the form $P = aT_s + b$ (with also two parameters, as PEM2) produces a smaller correlation of 0.69. The difference in the correlations is weakly significant with a p-value of 0.08, considering the effective spatial degrees of freedom following Bretherton et al. (1999), indicating that our non-linear model is structurally better than the linear model.

A somewhat unexpected success of the PEM is its ability to reproduce the southern hemisphere ITCZ in the eastern Pacific, which results from the nonlinear rectification of the seasonal cycle on the mean (see Sect. 4.2). However, PEM strongly underestimates P in the other tropical convergence

zones (by up to 40% in the eastern Pacific ITCZ), most likely due to the neglect of the effect of moisture convergence that enhances P in these regions (e.g. Back and Bretherton 2009a, b). The subtropical portion of the South Pacific convergence zone (SPCZ) is also likely not reproduced because it depends on synoptic-scale midlatitude systems (Widlansky et al. 2010). On the other hand, P is overestimated in the Caribbean and Arabian seas, associated with the high values of T_s above T_c (Fig. 8a). It also overestimates P on the northeastern edge of the SPCZ, where T_s is high, but the dry easterly inflow suppresses convection (Takahashi and Battisti 2007b; Lintner and Neelin 2008). The PEM2 has a reduced negative P bias over very high SST relative to PEM (Fig. 1c), but this does not necessarily mean that PEM2 is better, but rather that it has another bias that compensates for the missing wind convergence physics.

The frequency distribution of the observed monthly T_s (AMIP-SST; using 0.25 °C bins) is negatively skewed (e.g. Wallace 1992) and with a mode at 28°C (Fig. 1d), above which the frequency drops abruptly, with less than 1% of the data points for $T_s \geq 30$ °C (5% for $T_s \geq 29$ °C). Consistent with previous reports, the values of P (GPCP, 1979–2008) averaged for each T_s bin remain low below 22 °C, increase with T_s slowly at first up to 26 °C and then sharply up to 29 °C, above which they decrease rapidly. The PEM describes well this trend, although by construction it underestimates P for T_s below 26 °C (Fig. 1d). The spread of P for a given T_s (separation between percentiles) is approximately proportional to the mean P (Fig. 1e). The maximum spread can be seen increasing from 26 to 29 °C, as in some regions P increases with T_s as shallow convection gives way to deep

Table 3 PEM parameters for different combination of observational datasets and the spatial correlation R between the mean observational and corresponding PEM P distributions

Combination	Period	T_c	T_{p90}	$a1$	$a2$	R PEM	R PEM2
OISST–TRMM	1998–2015	26.01	29.60	66.18	-38.00	0.80	0.80
OISST–GPCP	1982–2015	25.50	29.60	49.82	-45.12	0.78	0.78
OISST–CMAP	1982–2015	25.74	29.60	63.95	-41.99	0.82	0.81
ERSST–TRMM	1998–2015	25.99	29.60	64.52	-27.20	0.75	0.76
ERSST–GPCP	1979–2008	25.43	29.40	50.66	-26.86	0.66	0.66
ERSST–CMAP	1979–2008	25.74	29.40	66.20	-13.12	0.73	0.73
AMIPSST–TRMM	1998–2008	25.39	29.3	60.79	-67.98	0.73	0.75
AMIPSST–GPCP	1979–2008	24.91	29.1	47.16	-45.88	0.76	0.74
AMIPSST–CMAP	1979–2008	25.18	29.30	61.88	-83.49	0.80	0.79
HadISST–TRMM	1998–2015	25.87	29.70	63.45	-86.02	0.77	0.76
HadISST–GPCP	1979–2008	25.36	29.50	48.41	-51.45	0.70	0.70
HadISST–CMAP	1979–2008	25.58	29.50	63.16	-46.70	0.76	0.75

The reference datasets in bold

convection while, in other regions, unfavorable large-scale atmospheric circulation does not allow such deep convection to develop effectively despite the increased T_s (Graham and Barnett 1987; Zhang 1993; Lau et al. 1997; Parsons et al. 2000).

4.1 PEM parameter fitting with different observational datasets

Although observational data products are often referred to as “observations”, any gridded fields that are complete in space and time are the result of sparse observations of different kinds (in situ, satellites) integrated and completed by diverse methods, so differences are to be expected among these products.

Here we assess the sensitivity of the results when fitting the PEM to different combinations of the observational products for P (GPCP, TRMM and CMAP) and T_s (AMIP-SST, ERSST, OI SST, and HadISST). Since these products are available for different time-periods, we assess the sensitivity by considering the following three periods: 1998–2008 (11 years), 1998–2015 (18 years) and 1979–2008 (30 years).

The tropical (20°S – 20°N) and time mean P and T_s (\bar{P} and \bar{T}_s , respectively) and their space-time standard deviations (σ_P and σ_{T_s} , respectively) vary substantially among the datasets, with CMAP producing about 15% higher \bar{P} than GPCP, consistent with previous studies (Yin et al. 2004) and TRMM shows the highest σ_P (Fig. 2a) while \bar{T}_s from AMIP-SST is about 0.3, 0.4, and 0.5 °C lower than HadISST, ERSST, and OI SST, respectively (Fig. 2a). The differences of both \bar{P} (1–2%) and \bar{T}_s (0.1–0.2 °C) are relatively small across time periods (Fig. 2b).

Both the mean and the median value of T_c , considering all products and periods, is 25.6 °C and the largest departures from this value correspond to the AMIP-SST product, which yields an average T_c of 25.16 °C. Furthermore, the post-1998 periods result in T_c about 0.2 °C larger than 1979–2008. In general, \bar{T}_s is higher than T_c in all the combinations, with larger $\bar{T}_s - T_c$ for GPCP (around 1.8 °C) and smaller for TRMM (around 1.2 °C).

The mean and the median values of a_1 across periods and datasets are 58.85 and 62.5 mm/°C, respectively, with the largest departures corresponding to the GPCP product, for which the a_1 parameter is around 23% smaller than for the other datasets (Table 3; Fig. 2c). As could be expected, the value of a_1 is approximately proportionally to σ_P , although the relationship depends on GPCP being somewhat of an outlier (Fig. 2c).

We find that the time-period does not have a substantial effect within each combination. Therefore, we use the longest period for each data combination, the fitted PEM parameters are summarized in Table 3. The spatial correlations

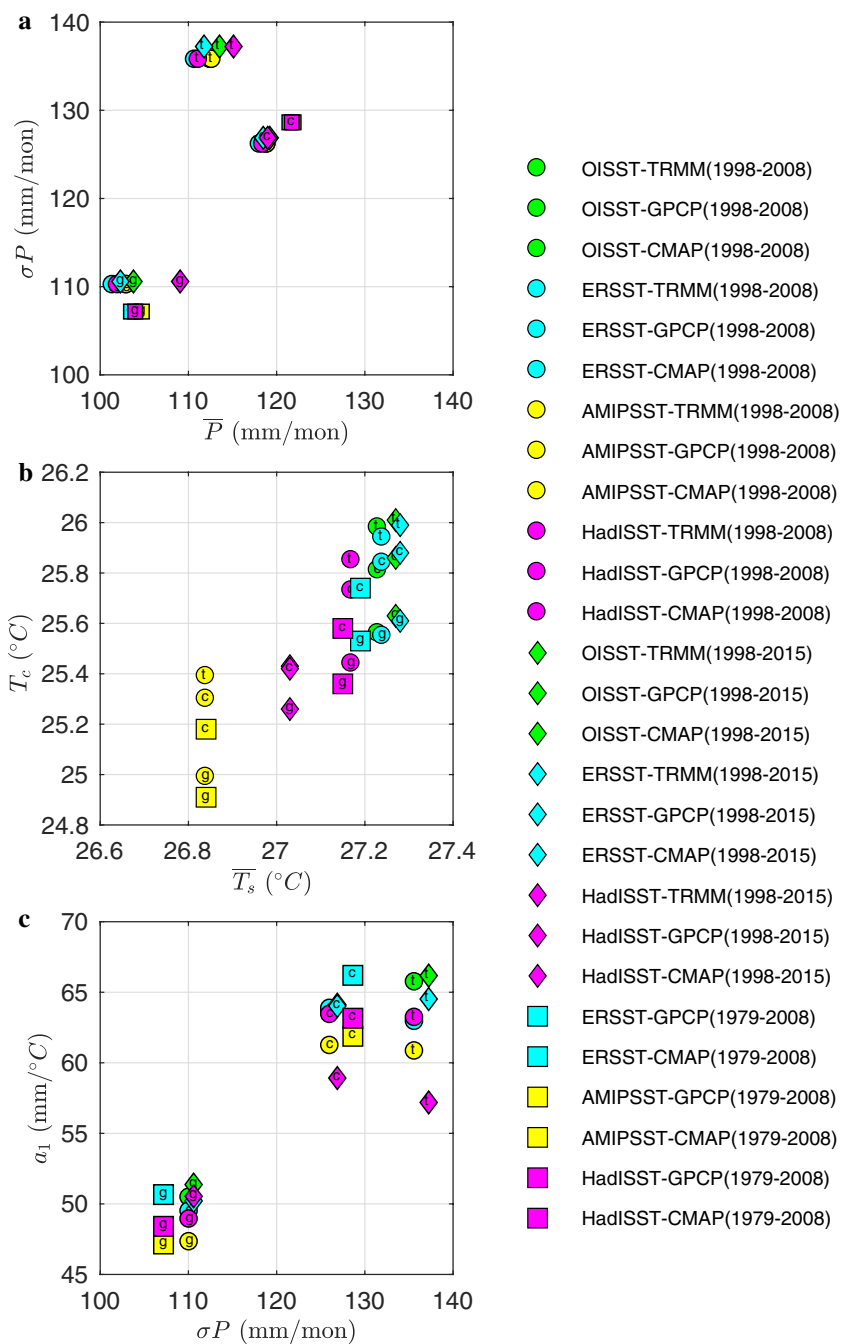
(0.7–0.8) show that PEM reproduces the mean spatial distribution of P relatively well for the different combinations of products.

4.2 Seasonal and interannual variability

We use the AMIP-SST/GPCP combination as our reference; however, our conclusions are not sensitive to the choice. The PEM produces time-varying monthly P fields given the T_s . The coefficient of determination (R^2) between the observational and PEM results for each grid point is a measure of the goodness of fit (percentage of the variability of P that is explained by the PEM). The result for the monthly data for the full period shows best results ($R^2 > 50\%$) over the eastern equatorial Pacific and the equatorial and tropical north Atlantic, particularly off the coast of northern Peru and southern Ecuador (Fig. 3a). If we repeat this calculation using only the climatological T_s and P , the pattern of R^2 is intensified (Fig. 3b), with high R^2 along $\sim 10^{\circ}\text{N}$, in accordance with the northernmost seasonal location of the ITCZ, and a band of high R^2 along the equatorial Atlantic and in the eastern Pacific just North of the equator, in accordance with the southward displacement of the ITCZ. The high values in the southeastern Pacific correspond to the formation of the secondary ITCZ in March–April (e.g. Huaman and Takahashi 2016), and the high values in the tropical southwest Pacific and South Indian oceans are linked to the development of the SPCZ and the broad southern ITCZ, respectively, in austral summer.

The seasonal cycle of P is described as a northward or southward movement of the precipitating regions that are located in the regions of highest T_s , which in turn follow the march of the sun (Mitchell and Wallace 1992). Deep convection in the eastern half of the Pacific is confined to the ITCZ north of the equator, which has a northernmost position around September, except for a brief period during March–April in which a double ITCZ appears straddling the equator (Zhang 2001). September is also near the peak of the Asian monsoon (Wang et al. 2009; Li and Zhou 2011). Thus, to characterize the seasonal difference of rainfall we consider the difference between the climatological P for September and March, although similar results are found using JJAS minus DJFM as a seasonal cycle. The comparison between the observational data (Fig. 4a) and the result from the PEM (Fig. 4b) is good, with a spatial correlation of 0.64. As expected given the weakness of the modeled convergence zones, the dipolar pattern resulting from their meridional displacements is not as strong as observed. Similarly, the rainy signal in the northern Indian Ocean linked to the Asian monsoon in September is not depicted by the PEM. In the western half of the equatorial Pacific (Fig. 4b), the PEM produces a weak seasonality with the

Fig. 2 Scatter plot between: **a** P and σP , **b** T_s and T_c , **c** σP and the slope (a_1). Circles are for 1998–2008 (11 years), diamonds for 1998–2015 (18 years) and squares for 1979–2008 (30 years). Colors indicate T_s datasets: green for OISST, cyan for ERSST, yellow for AMIP and fuchsia for HadISST. Lowercase letters inside each marker indicate P 's datasets: g for GPCP, t for TRMM, and c for CMAP



sign opposite to observed. This is a permanently convective region ($T_s > T_c$) with a weak seasonal range in T_s ($\sim 0.5^\circ$ C), so the dynamical processes most likely play a dominant role in the seasonality here (Holland and Keenan 1980; Williams and Houze 1987; Tompkins 2001; Yang and Slingo 2001; Saito et al. 2001; Neale and Slingo 2003).

The interannual variability is dominated by El Niño–Southern Oscillation (ENSO). The P variability is particularly pronounced in the equatorial eastern Pacific, where the mean conditions are stable ($T_s < T_c$) but extreme El Niño increase T_s strongly above T_c (Takahashi

and Dewitte 2016). In agreement, high correlations ($R^2 > 0.8$) are found in the far eastern Pacific, particularly off the coasts of southern Ecuador and northern Peru, between the P anomalies in GPCP and the associated PEM (Fig. 3c). For comparison with climate models, we quantify the goodness of fit to the ENSO variability by considering the longitude-time R for the monthly equatorial (5°S–5°N average) eastern Pacific (150°W–80°W, not zonally averaged) P anomalies for the 1979–2008 period, which takes the value of 0.77.

Fig. 3 Coefficient of determination between P from observation and P estimated by PEM in **a** monthly, **b** monthly climatology and **c** annually from 1979 to 2008

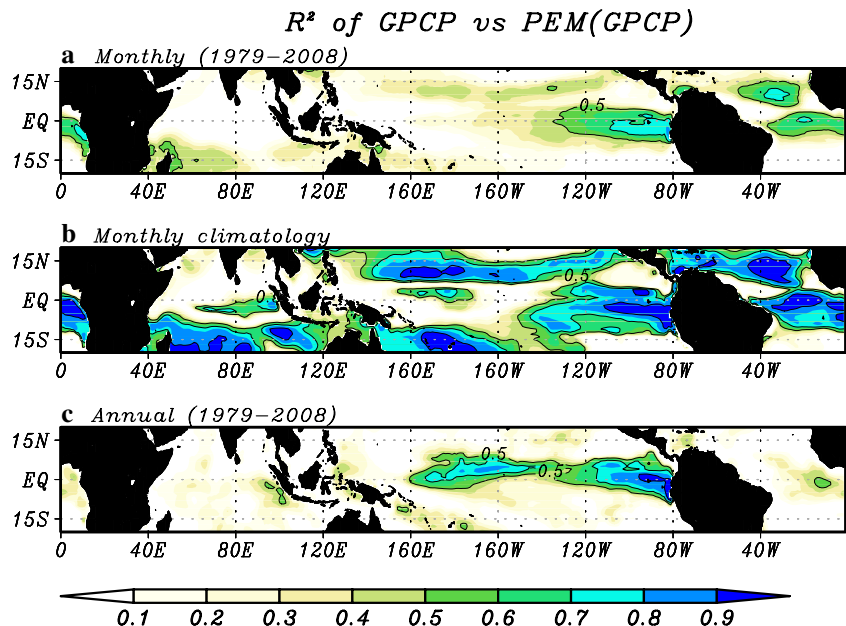
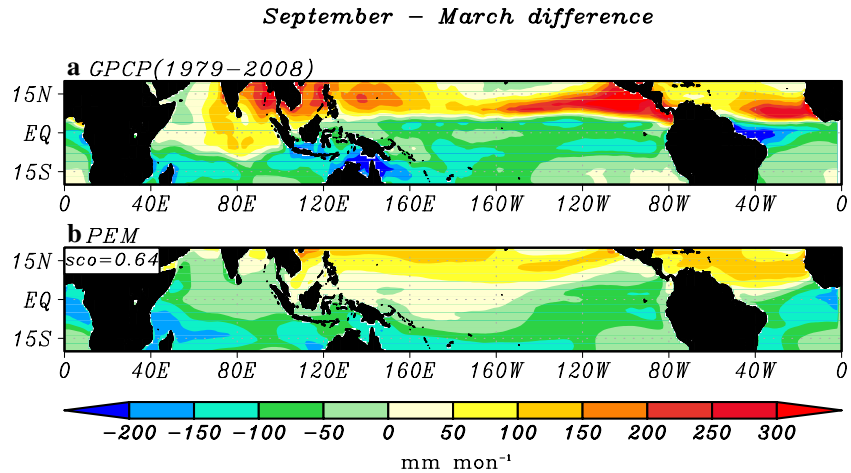


Fig. 4 Maximum seasonal difference of rainfall (September minus March) for **a** observational data and **b** estimated by PEM



5 Application of the PEM to the global climate models

5.1 Present climate and model intercomparison

All of the GCMs and experiments (AMIP, HIS, RCP4.5) show a nonlinear relationship similar to the observed (for example, Fig. 5), with a gradual increase of P with T_s up to T_c , followed by an abrupt increase between T_c and T_{p90} , and the decrease of P above the latter. For some GCMs/experiments, the 90-percentile of P binned by T_s did not present a sharp peak corresponding to T_{p90} , which affected the estimation of a_2 resulting in positive values in some cases (e.g. CESM1-CAM5; Fig. 5b). The resulting 95% confidence interval is of the order of 0.4% for T_c , 5% for a_1 and 40%

for a_2 for the HIS, AMIP and RCP4.5 experiments. Therefore, the estimated sampling error is small for T_c and a_1 ; however, the uncertainty of a_2 is high because it is affected by T_{p90} . Some GCMs presented few very high values of T_s ($>35^\circ\text{C}$) but with little associated P (e.g. Fig. 5c).

The spatial correlations between \bar{P} from the GCMs (HIS and AMIP) with \bar{P} from PEM indicate a generally good representation, with values of $R \geq 0.7$ generally higher to that obtained with the observational data (red bar), except for the GISS models, which had values $R \geq 0.6$ (Fig. 6a). For the seasonal pattern (September minus March) of P , the spatial correlations for all (HIS) GCMs are ≥ 0.6 , also generally larger than for the observational data (Fig. 6b). Interestingly, the correlations for the seasonality are slightly smaller for the uncoupled (AMIP) than for

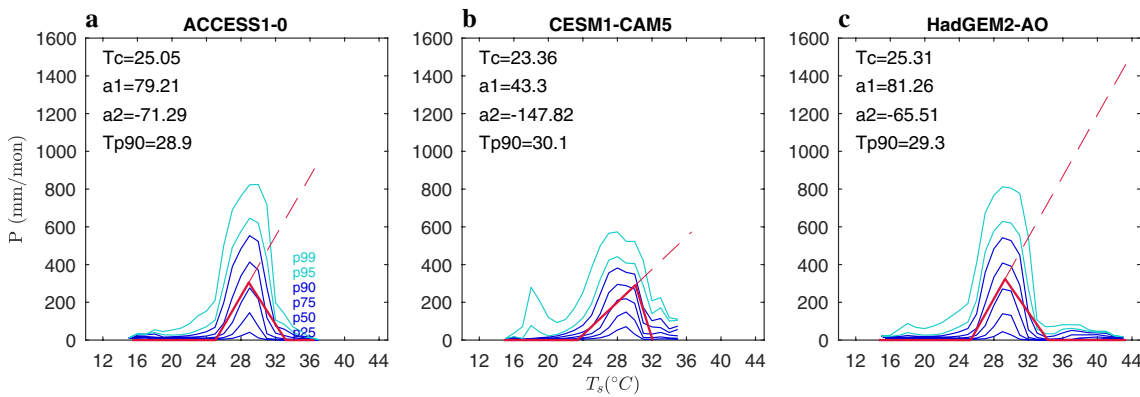
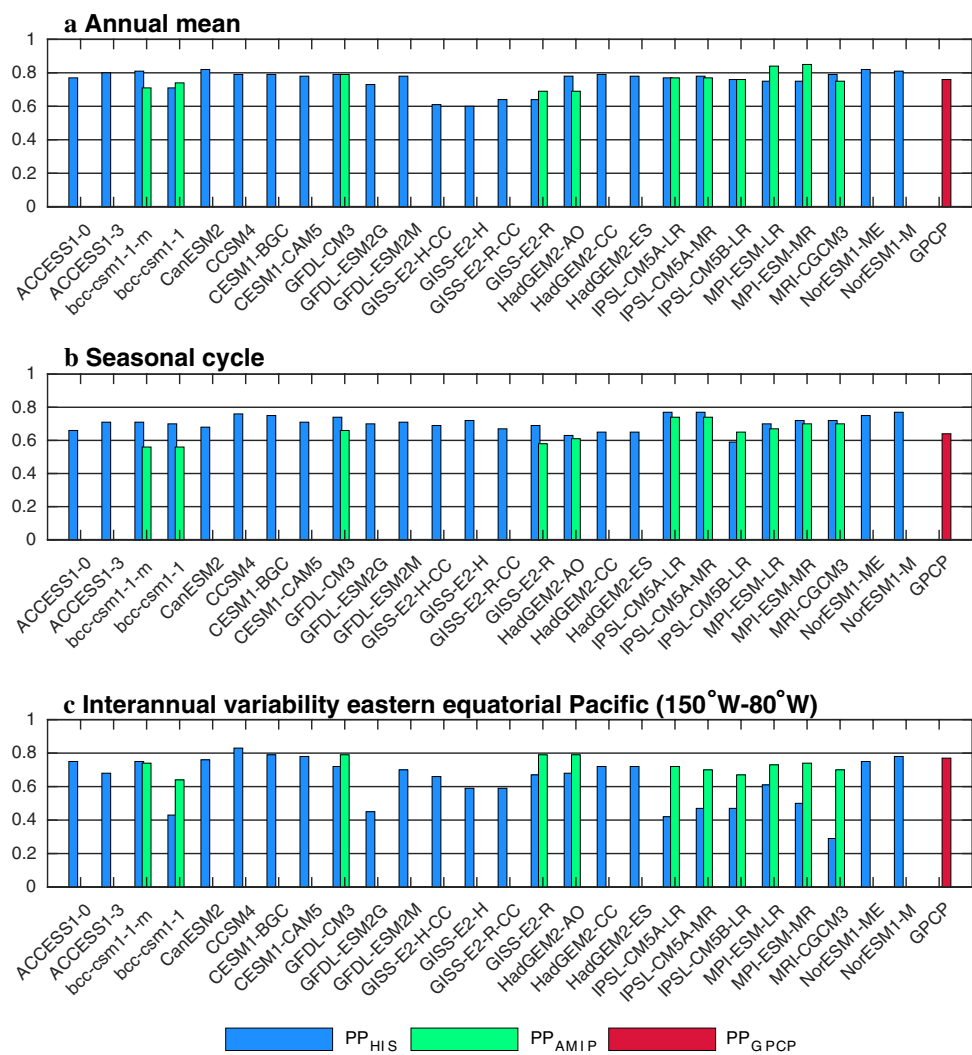


Fig. 5 Similar to Fig. 1d but for GCMs in the HIS experiments (1961–2000): **a** ACCESS1-0, **b** CESM1-CAM5, and **c** HadGEM2-AO

Fig. 6 Linear correlation coefficients between P from GCMs (HIS in blue, AMIP in green) and from the PEM fitted to them. Spatial correlations are shown for the **a** annual-mean, **b** seasonal cycle, as well as **c** longitude-time correlation for monthly equatorial (5°S – 5°N averaged) eastern Pacific (150° W– 80° W, not averaged). The observational estimate using GPCP (1979–2008) is shown in red



the coupled GCMs, particularly for bcc-csm1-1-m, bcc-csm1-1 and GISS-E2-R. For the interannual variability of the eastern equatorial Pacific, mainly driven by ENSO, the longitude-time correlations are >0.4 for all GCMs

except for the MRI-CGCM3 coupled model (Fig. 6c). For the observational dataset the correlation is 0.77 and some coupled GCMs exceed this (e.g. CCSM4, CESM1-BGC, CESM-CAM5, NorESM1-M), although the values vary

substantially among the GCMs (Fig. 6c). The uncoupled GCMs are more consistent in presenting high correlations, indicating that even though the atmospheric components represent the P response to the ENSO T_s anomalies, the coupled phenomenon is not as well represented, particularly in the eastern Pacific (e.g. Dewitte and Takahashi 2016).

The multi-model ensemble (MME) mean of P and T_s from GCMs, 26 for the HIS and 11 for the AMIP experiments (Fig. 7a, c) match their corresponding PEM results (Fig. 7b, d), with a spatial correlation around 0.82 and 0.83, respectively. However, it is perhaps more illustrative to analyze the biases in P in the GCMs and PEM. Several of the GCM's best-known biases are represented by the PEM (Fig. 8b, c). For example, the excessively zonal SPCZ (Brown et al. 2011, 2013), the excessive P in the southeast Pacific due to the double ITCZ bias (Mechoso et al. 1995; Yu and Mechoso 1999; Meehl et al. 2005; Dai 2006; Lin 2007; de Szoeke and Xie 2008; Zhang et al. 2015), particularly along the coast of South America (Davey et al. 2002), as well as in the south Atlantic ocean (Biasutti et al. 2006; Stockdale et al. 2006; Richter et al. 2014; Siongco et al. 2014). The main discrepancy, noted before, is the strong underestimation by the PEM of P in the (north) eastern Pacific ITCZ. The PEM also does not simulate the dry bias in the western equatorial Pacific which is linked to equatorial Pacific cold tongue extending too far west (Li and Xie 2014). A more subtle difference is that the wet bias in the southeast Pacific is less zonal in the PEM, in conformity

with a role for coupled dynamical processes to amplify the double ITCZ bias (Lin 2007; de Szoeke and Xie 2008).

For the uncoupled AMIP experiment, the mean P bias of the GCMs (Fig. 8d) is approximately reproduced by the PEM (Fig. 8e), particularly the wet bias in the north Indian ocean, the off-equatorial central-western Pacific, off the coast of northern South America, and south of the equator in the Atlantic, as well as the dry bias north of the equator in the Atlantic. Interestingly, the bias of PEM fitted to the AMIP runs (Fig. 8e) is more similar to what the PEM produced for the HIS experiment (Fig. 8c) than to the AMIP models themselves (Fig. 8d), most notably in the eastward projection of the wet bias associated with the SPCZ. On the other hand, the main difference between the PEM for HIS and AMIP experiments is the larger wet bias in the south-eastern Pacific and Atlantic in the PEM for HIS than for AMIP, congruent with P and the warmer T_s in the former in those regions (Figs. 8c, e, 7a, c).

The difference between the time/space-mean T_s and the critical temperature, i.e. $\bar{T}_s - T_c$, provides a measure of the tropical convective instability and it could be expected that the GCMs with larger values would produce stronger mean P biases. The inter-model correlation reflects this to some degree (Fig. 9), with values around $R = 0.6$ coinciding with the regions of positive biases in the HIS experiments (Fig. 8b). This is consistent with previous findings that models with a larger excess of T_s over their corresponding convective thresholds are more prone to the double ITCZ bias (Bellucci et al. 2010; Oueslati and

Fig. 7 Annual-mean precipitation (shaded) and mean T_s (contours) for the multi model ensemble (MME) from **a** 26 GCMs from the HIS simulation, **b** PEM from 26 GCMs (HIS) **c** 11 GCMs from AMIP and **d** 11 PEM from GCMs (AMIP)

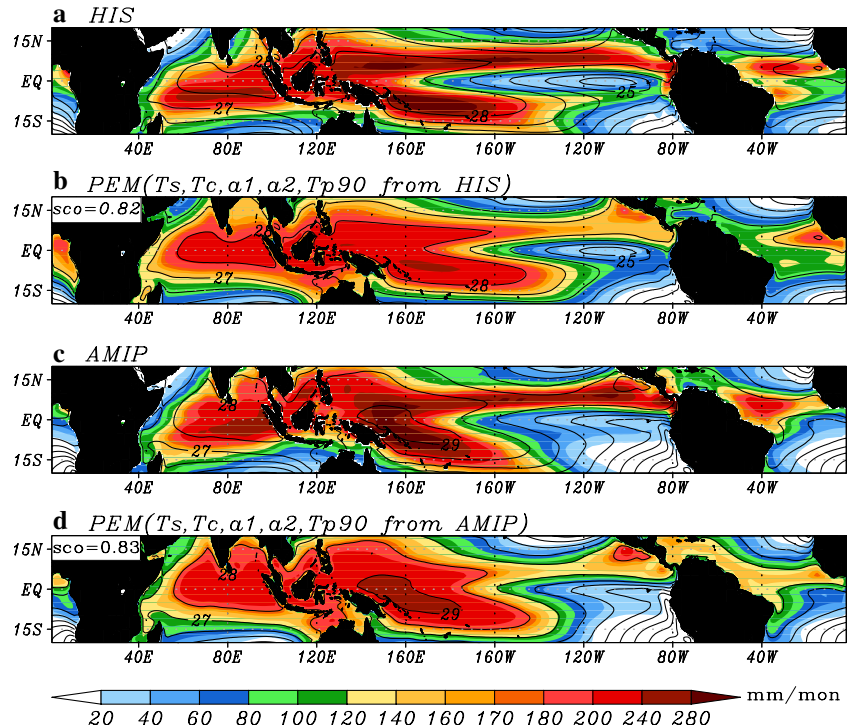


Fig. 8 **a** Rainfall mean error relative to GPCP (1979–2008) for **a** PEM (GPCP-AMIPSST), **b** MME from HIS, **c** MME from PEM (HIS), **d** MME 11 AMIP, **e** MME from PEM (AMIP)

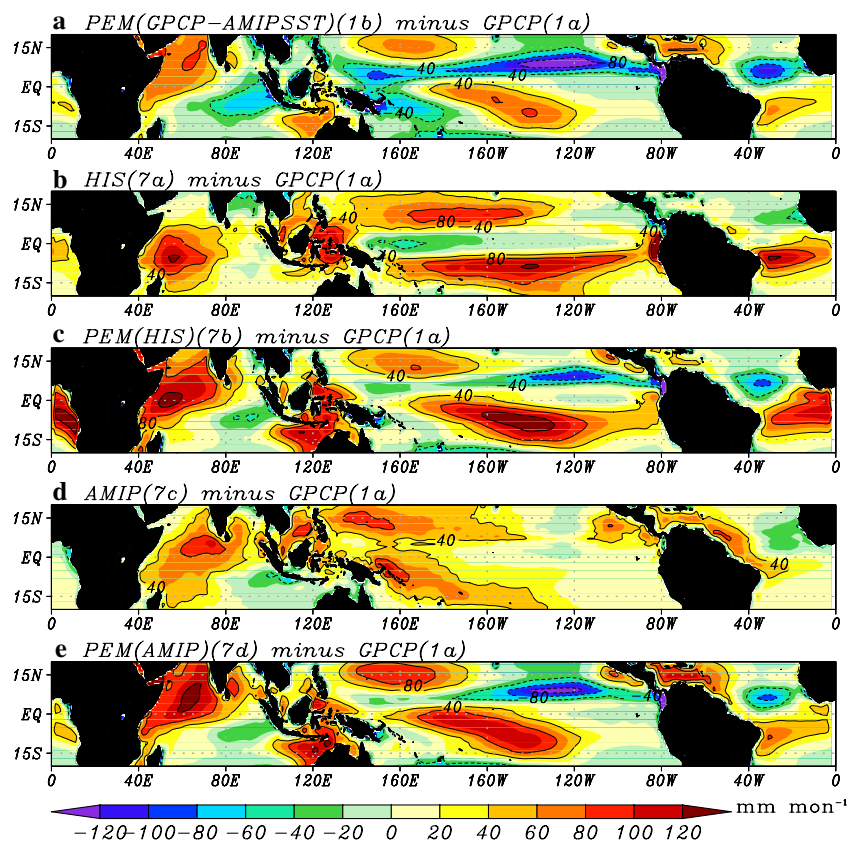
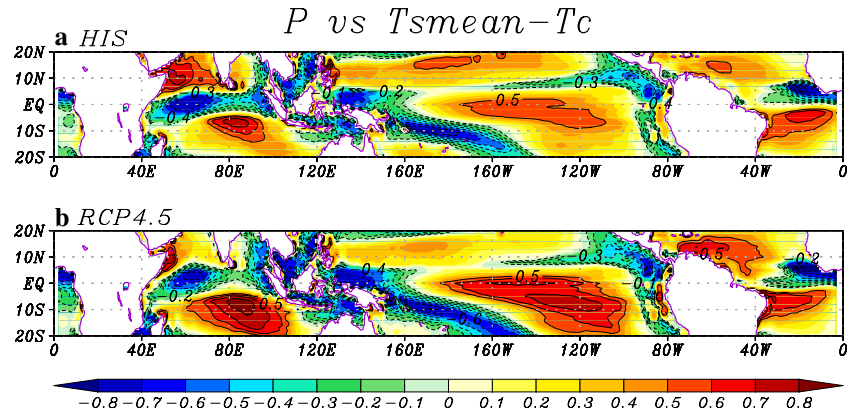


Fig. 9 Inter-model correlation between the annual mean P and the tropical/annual mean $T_s - T_c$ for the **a** HIS and **b** RCP4.5 experiments

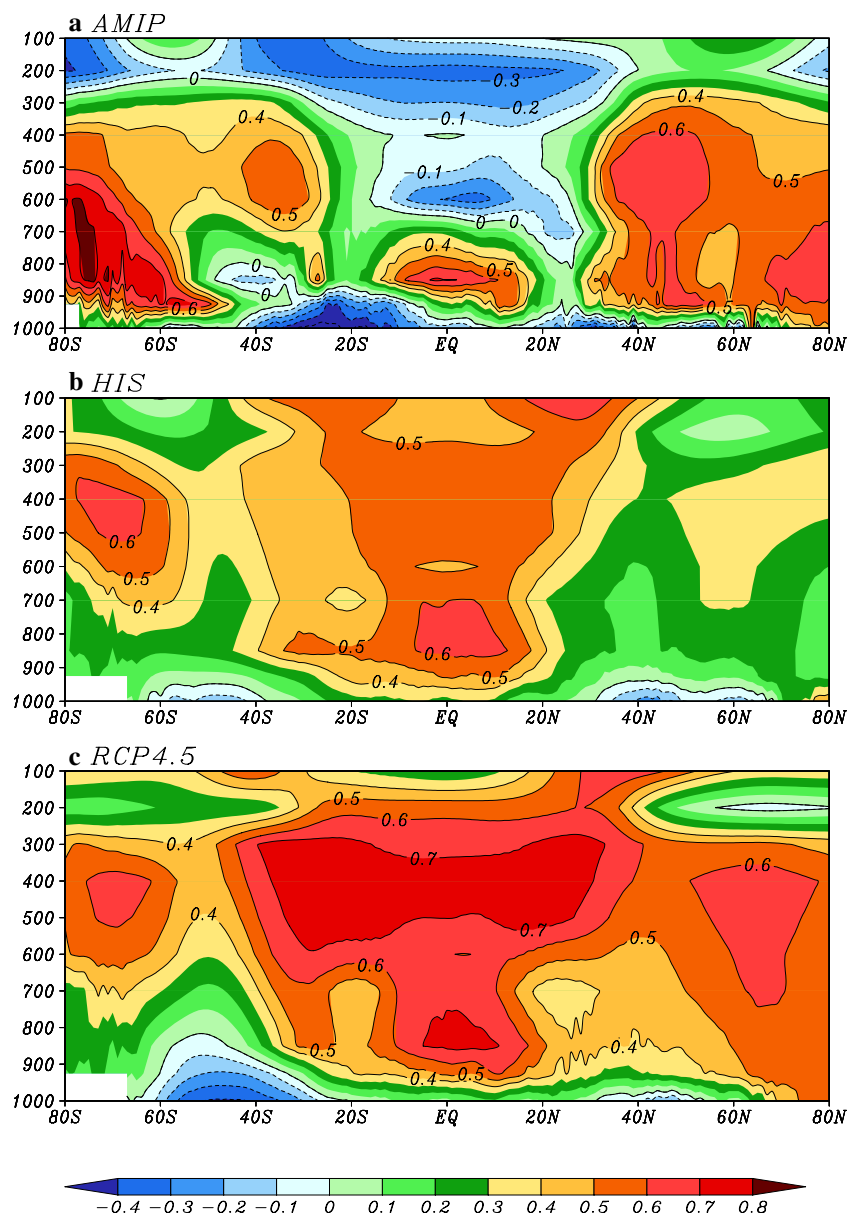


Bellon 2015). We note that this R distribution is roughly zonally symmetric, with positive values off the equator in all oceans, and negative values in the poleward flank of the SPCZ, the equatorial Indian and Atlantic oceans and on the Maritime Continent, i.e. points to a general tropical problem, rather than to regional processes, underlying the double ITCZ bias.

To test the theory that increased T_c is linked with the stabilizing effect of higher free tropospheric temperature (e.g. Johnson and Xie 2010) but among models rather than in time, we calculate the inter-model correlation between

the temporal/zonal mean air temperature and the T_c values. We find that in the tropics, for the coupled GCMs (HIS and RCP4.5) the correlation is small near the surface and is highest in two free-troposphere layers: 850–700 and 600–300 hPa (Fig. 10b, c). Comparing the temperatures at the two levels for all experiments and the observational data shows that the cold tropospheric bias in the GCMs (Tian et al. 2013) provides a reasonable explanation for the negative bias in T_c (more clear relative to ERSST and the other T_s products than to AMIP-SST; Fig. 11).

Fig. 10 Inter-model correlation coefficient between annual-mean zonal-mean T_a and T_c for the **a** AMIP, **b** HIS and **c** RCP4.5 experiments



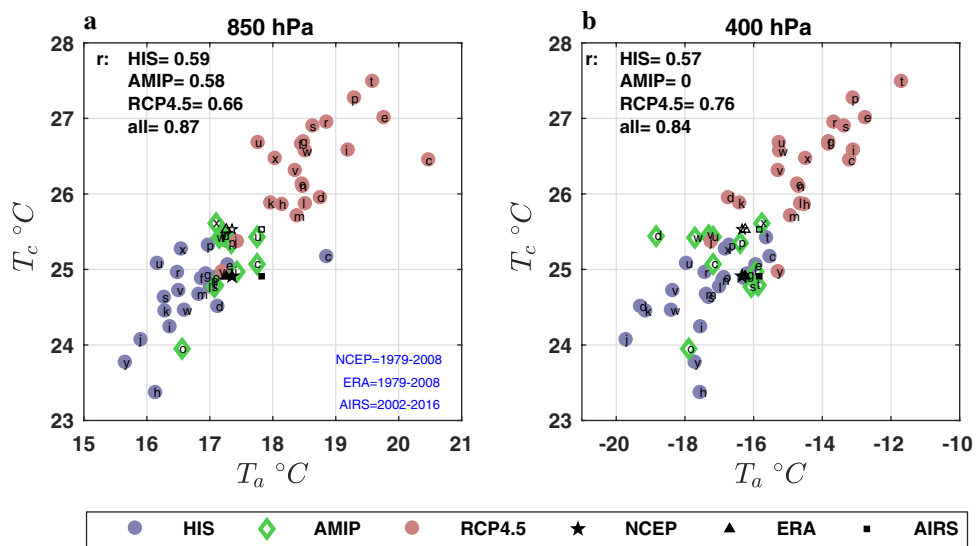
The high correlation in the upper troposphere is in agreement with the findings of Johnson and Xie (2010) who find a high correlation between T_c and 300 hPa temperature, but this is conceptually puzzling since although the upper troposphere temperature affects CAPE, it does not necessarily impose a particular threshold. To test the possibility that this correlation is spuriously reflecting the variability of the reference temperature associated with the spatial mean \bar{T}_s , we repeat the same calculation but after first subtracting \bar{T}_s from T_a and T_c . We find that the upper-troposphere correlations disappeared, leaving only the positive values around 850 hPa around the equator (Fig. 12), reaffirming the interpretation in terms of convective inhibition (CIN), i.e. that $T_s - T_c$ is a measure of low-level stability that has to be overcome in order for the incipient convection to tap into

the convective available potential energy (CAPE). We note that the correlations for the AMIP experiment alone are not robust (Figs. 10a, 11), not only due to substantially smaller values than for the coupled models but also, if we remove the GISS-E2-R model, the positive correlation at 850 hPa is strongly reduced (not shown).

5.2 Climate change effects

Simulated changes in the tropical precipitation (ΔP) distribution under future climate change scenarios generally feature increase in the equatorial Pacific and Indian oceans, and decrease over much of the subtropical oceans (Collins et al. 2013). This is also shown for the RCP4.5 (2061–2090) relative to the HIS (1971–2000) experiments (Fig. 13b), in

Fig. 11 Scatter plot between T_a (20°S – 20°N averaged) against T_c for HIS (blue circles), AMIP (green diamonds), RCP4.5 (red circles) and observations (black markers) with AMIPSST (filled) and ERSST (open) for **a** 850 hPa and **b** 400 hPa



which we see the largest absolute increase in the equatorial Pacific. This is approximately represented by the PEMs (spatial correlation of 0.6), although they underestimate the increase in the equatorial Pacific and overestimate the drying in the southern tip of the SPCZ (Fig. 13c, d). The highest spatial correlations (≥ 0.6) between ΔP from the GCMs and their fitted PEMs are presented by ACCESS1-3 and IPSL-CM5A-LR (PEM2 yields similar results).

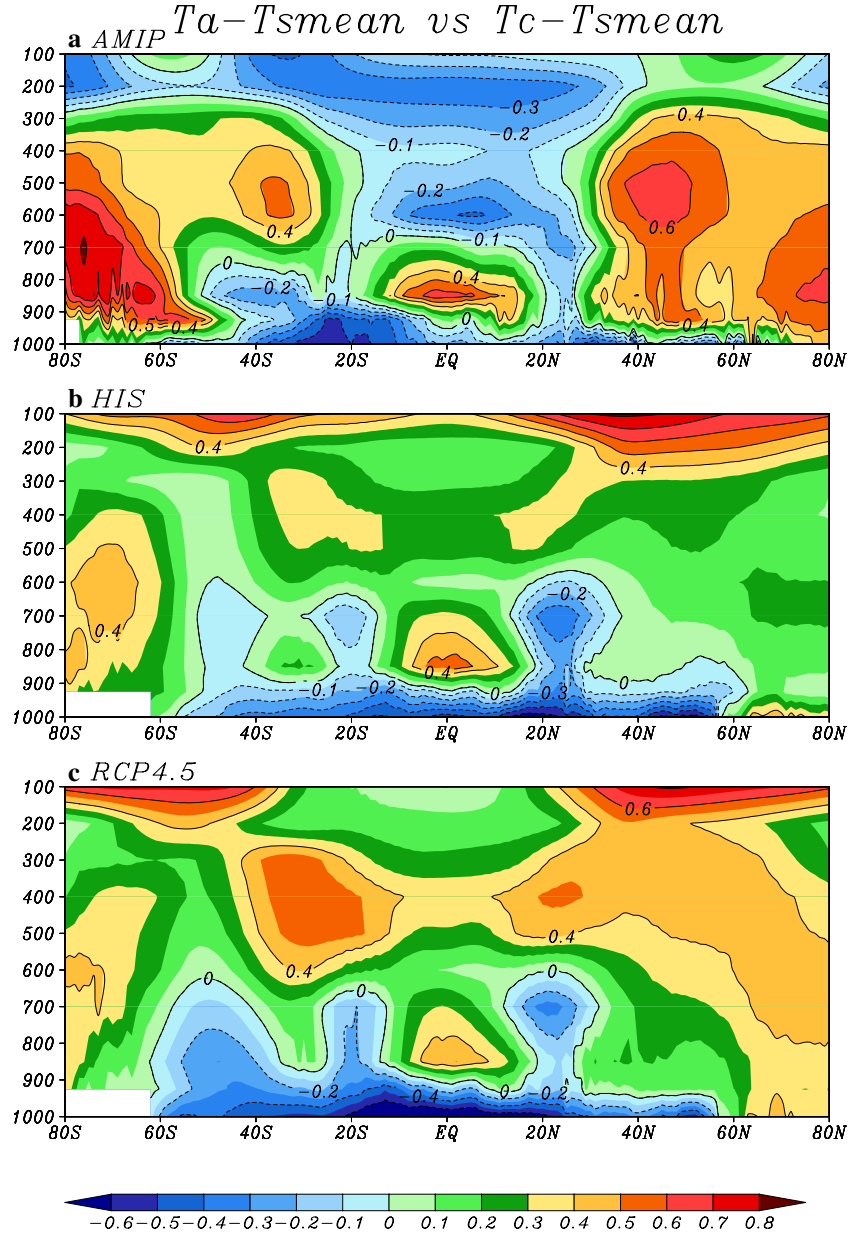
In most of the tropics, $\Delta(T_s - T_c)$ is negative (-0.2°C) in the tropical mean; Fig. 2b in Johnson and Xie 2010), consistent with the enhanced stability associated with the free troposphere warming following a moist-adiabatic lapse rate in the GCMs (Collins et al. 2013). The pattern follows that of ΔT_s , featuring an El Niño-like zonal gradient (Ramanathan and Collins 1991; Meehl and Washington 1996; Collins 2005; Vecchi and Soden 2007a; Song and Zhang 2014), an enhanced equatorial response (EER) in the Pacific (Seager and Murtugudde 1997; Liu et al. 2005; Xie et al. 2010; Ma and Xie 2013), and a hemispheric asymmetry with more warming over the north than the south hemisphere (Xie et al. 2010; Sobel and Camargo 2011; Friedman et al. 2013). Although this surface pattern plays a key role in rainfall projection through the warmer-get-wetter mechanism (Xie et al. 2010; Zhang and Li 2014), it varies across scenarios (DiNezio et al. 2009) and models (Ying et al. 2015). The largest decreases in $T_s - T_c$ are found in the southeast Pacific and South Indian tropical oceans and relatively weak increases in the eastern equatorial Pacific and northeastern Indian Ocean (Fig. 13a).

The fact that the PEMs simulate generally positive mean ΔP in the equatorial region despite the largely negative $\Delta(T_s - T_c)$ is due to the increase in the a_1 coefficient, which increases by 27%/K on average with T_s but with a range of 9–49%/K given by the 10 and 90 percentiles. This is much larger than the Clausius-Clapeyron scaling for specific

humidity, which is on the order of 7%/K (Held and Soden 2000) and the increase in extreme precipitation of 6%/K (4–10%/K range) with climate change in CMIP5 models (Kharin et al. 2013). It is, however, in agreement with the increase in the sensitivity of P to El Niño T_s anomalies (Cai et al. 2014). We note that our error estimate for the fit of the absolute a_1 is an order of magnitude smaller than its mean difference between experiments.

The pattern of ΔP produced by the PEMs can be understood in terms of the competing effects of the negative $\Delta(T_s - T_c)$ and positive Δa_1 , but restricted to convective regions by the absolute value of $T_s - T_c$ (Liu et al. 2005; Xie et al. 2010; Lu and Zhao 2012). An interesting example of this is the off-equatorial location of the maximum ΔP in the central and eastern Pacific in GCMs (Fig. 13b), on the equatorial flanks of the ITCZs in both hemispheres. This feature is also present in the previous generation of GCMs. It is not represented by the simple moisture-based “wet-gets-wetter” theory (Held and Soden 2006) but has been diagnosed in terms of dynamical changes (e.g. Chadwick et al. 2013). This double-band structure has a strong seasonal component linked to the excessively strong double ITCZs in the GCMs, so the P increase is strongest in the summer-fall hemisphere (Dec-May in the south, Jun-Nov in the north; Fig. 14a). Both PEMs reproduce this feature (Fig. 13c, d) and provide a first-order parsimonious and causal explanation for this structure in ΔP , which is that ΔP is largest due to the increased a_1 in the intersection of the regions where absolute $T_s - T_c$ is high (in the equatorial oceans excluding the cold tongue, approximately where $T_s - T_c \geq 2.2^\circ\text{C}$ and where $T_s - T_c$ decreases the least with climate change (around the cold tongue, e.g. $\Delta(T_s - T_c) \geq -0.2^\circ\text{C}$), as shown in Fig. 14b for the eastern Pacific where the PEM reproduces best the double-band structure of the P increase. This same explanation

Fig. 12 Similar to Fig. 10 but for zonal-mean $T_a - \bar{T}_s$ and $T_c - \bar{T}_s$

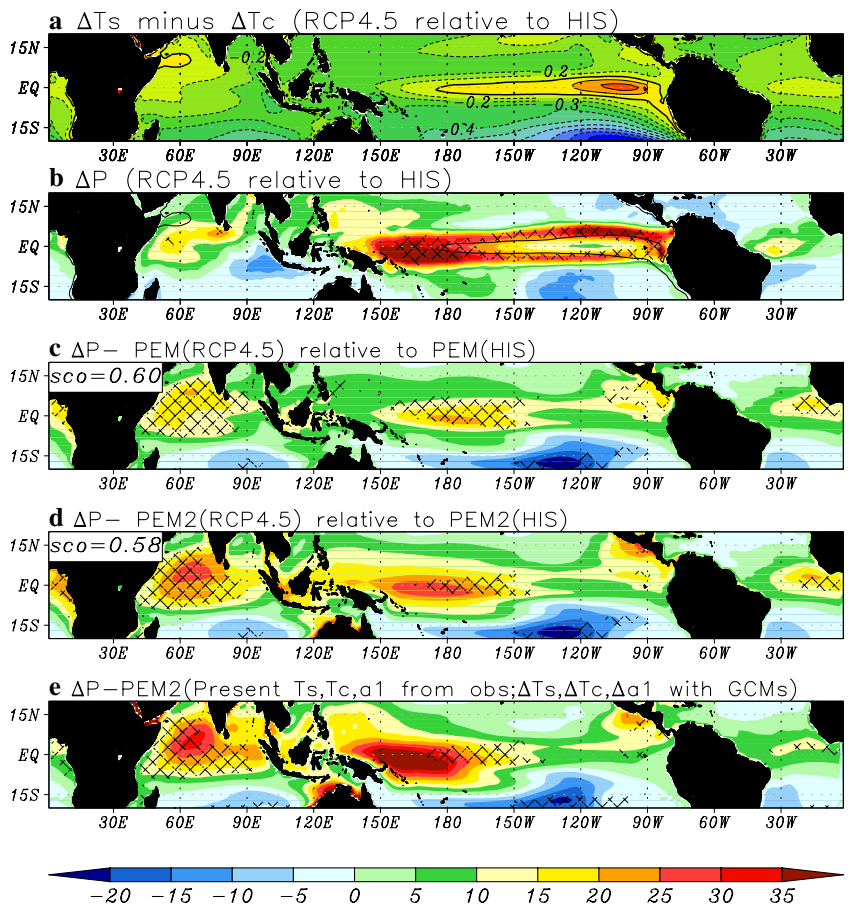


is valid for the high ΔP in the edge of the western Pacific warm pool along the equator, which is a convective region where $\Delta(T_s - T_c) \geq -0.2^\circ\text{C}$. In general, however, the PEM strongly underestimates the peak ΔP in these regions, probably due to the lack of dynamical feedbacks like the changes in moisture convergence. Furthermore, we do not at this point have a quantitative theory for Δa_l , but anticipate that it should involve dynamical feedbacks in addition to the thermodynamic component.

Since the eastern Pacific ΔP is strongly influenced by the double ITCZ bias in the GCMs, it is desirable to reduce the effect of the biases in the assessment of ΔP and we can do so in a straightforward way by using the PEMs fitted to the observational data and apply the changes in T_s and the PEM

parameters from the GCMs to obtain the future scenarios. As a result, the positive ΔP in the southeast Pacific and Atlantic is substantially reduced in the bias-corrected case (Fig. 13e) relative to the original PEM (Fig. 13d). Since $\Delta(T_s - T_c)$ is the same in both cases, the main difference is in the mean state $T_s - T_c$, which has substantially lower values in these regions than in the GCMs (Fig. 14c). The reduced ΔP off South America implies a reduced northerly component in the climate change signal on the low-level winds (Belmadani et al. 2013), which in turn would indicate a positive dynamical feedback on this reduction of ΔP . We should note that the strong ΔP in the southeast Pacific, particularly off Ecuador and northern Peru, is a robust signal among the GCMs (hatching in Fig. 13b), but is strongly

Fig. 13 Multi-model ensemble mean (MME) of projected annual-mean changes in: **a** $T_s - T_c$ for 2061–2090 relative to 1971–2000 under RCP4.5, **b** P from GCMs, **c** P estimated by c. PEM and **d** PEM2 fitted to GCMs, and **e** P with PEM2 using observed T_s and parameters, with the changes (HIS to RCP4.5) from GCMs. Hatching indicates areas where projected changes agree (24 out of 26) on the sign of change



reduced with the bias correction, consistent with the results with an atmospheric GCM with bias-corrected T_s (Ashfaq et al. 2011), warning us that the agreement between GCMs does not imply high certainty as shared biases affect them in the same ways, i.e. GCMs are not independent (Masson and Knutti 2011). Other effects of the bias-correction in the PEM are the reduction of ΔP in the Indian Ocean and in the eastern Pacific warm pool (Fig. 13e). The other major difference is the enhancement of ΔP in the edge of the western Pacific warm pool, which in the GCMs is further to the west due to the cold tongue bias, so the mismatch between the GCM $\Delta(T_s - T_c)$ and the observational $T_s - T_c$ patterns produces this spurious enhancement (Brown et al. 2015).

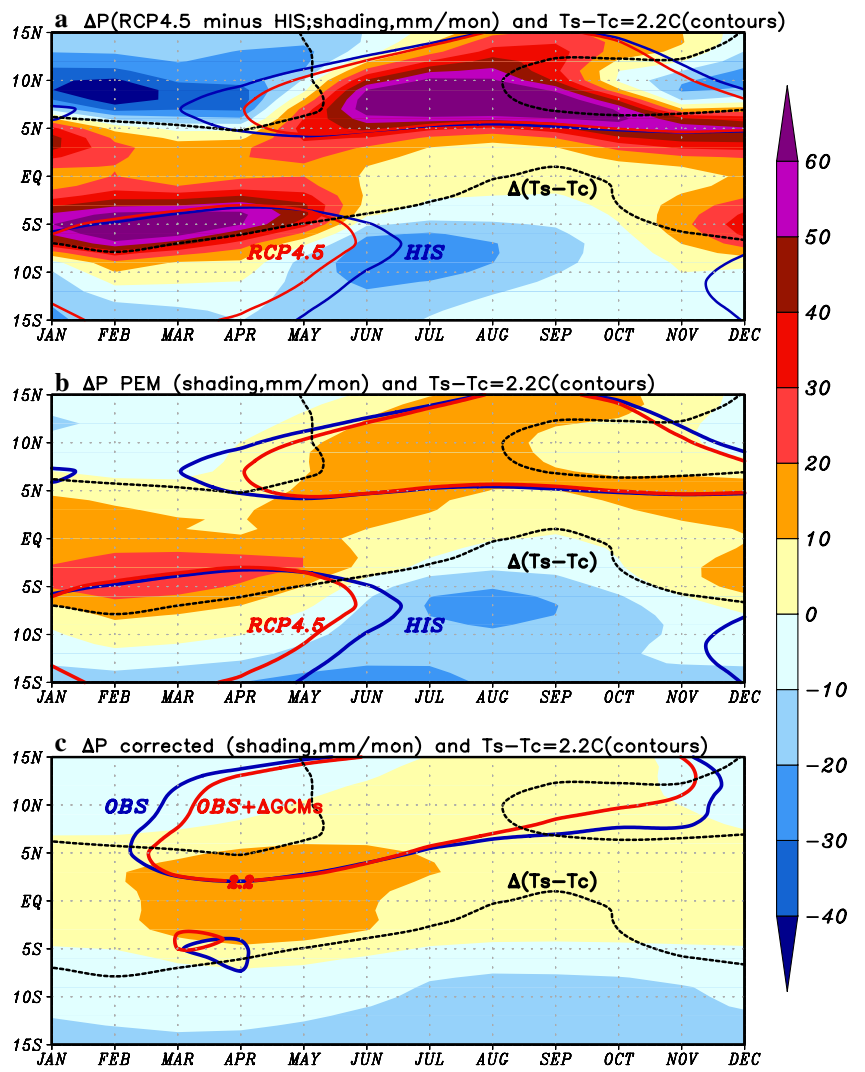
6 Conclusions and discussion

We have shown that a simple point-wise “physical-empirical model” (PEM), with only two constant parameters and given the sea surface temperature (T_s) provides a good first approximation to the monthly tropical precipitation (P) distribution, including the seasonal ITCZ in the Southeast Pacific, for both the observational data and GCMs.

However, it strongly underestimates the peak P in the convergence zones, consistent with the neglect of the effects of the atmospheric circulation. Conceptually the PEM is based on the idea that deep convection is limited by the convective inhibition (CIN) linked to the low-level tropospheric stability.

The PEM is also able to reproduce the biases of the GCMs, both coupled and atmosphere-only, particularly the excessive P in the off-equatorial Pacific, associated with the double ITCZ syndrome, and in the near-equatorial Indian Ocean. Interestingly, the biases of the PEM fitted to the observational data are similar to the biases of the atmosphere-only GCMs, like the generally excessive P , suggesting that the latter also misrepresent some of the physical processes active in nature. We show that after correcting the mean biases in the GCMs, our PEM strongly reduces the increase in P with climate change in the Southeast Pacific and Atlantic, which in the GCMs appears robust but is probably an artifact of the shared double ITCZ bias. Consistent with previous studies, we find that the excess of the tropical mean T_s over the critical value T_c for convection is correlated across GCMs with a pattern similar to the double ITCZ bias. The inter-model variability in T_c is linked with the variability in the near-equatorial low-level

Fig. 14 140°W–120°W mean monthly climatology of the change in P from HIS to RCP4.5 (shading, mm/month) and change in $T_s - T_c$ (black contour, only -0.2°C shown). Also shown are the $T_s - T_c = 2.2^\circ\text{C}$ contours for HIS (blue) and RCP4.5 (red). **a** is for the GCMs, **b** for the PEM adjusted to the GCMs, and **c** uses the observational T_s and PEM2 parameters, but the changes in the latter from the GCMs



(850hPa) tropospheric temperature, particularly after correcting for the inter-model differences in the reference T_s , consistent with the interpretation of $T_s - T_c$ as a measure of CIN or atmospheric stability. The underestimation in T_c by the GCMs appears to be associated with a cold bias at this level. We should note that the double ITCZ bias is also related with the tropical mean P (Lin 2007), which is controlled by processes not explicitly considered in the PEMs (e.g. global mean radiative fluxes (Takahashi 2009a, b) but would be implicit in the values of the fitted parameters (e.g. a_1), so the PEMs emulate the behavior of the atmospheric GCMs, not just their convective parameterization schemes.

Our PEM provides a parsimonious explanation of the pattern of ΔP associated with climate change. Even though $\Delta(T_s - T_c)$ is generally negative according to GCMs (except in the eastern equatorial Pacific and northwestern Indian oceans), ΔP is positive in the equatorial region due to the increase in the parameter a_1 that measures the sensitivity of P to T_s once it exceeds T_s . The

increase in a_1 is on the order of 10–50% per degree $^\circ\text{C}$ of surface tropical warming, in agreement with previous studies, leading to increased P where $\Delta(T_s - T_c)$ is less negative. However, P does not increase as much in the Pacific equatorial cold tongue, despite presenting the largest $\Delta(T_s - T_c)$, as it is a region where the absolute $T_s - T_c$ remains low. The double banded ΔP structure in the Pacific is associated with the equatorial flanks of the strong double ITCZs and is tightly linked to their seasonality. If we bias-correct the PEM, effectively removing the double ITCZ bias, the projections no longer present the strong ΔP in the southeastern Pacific and Atlantic oceans that is a consensus result among GCMs (Collins et al. 2013), emphasizing the need to explicitly assess the structural uncertainty in the climate change projections (IPCC 2005).

Acknowledgements The data used in this study were provided by the NOAA/OAR/ESRL PSD (GPCP, CMAP, OI SST, ERSST; <http://>

www.esrl.noaa.gov/psd/), Goddard Space Flight Center Distributed Active Archive Center (TRMM 3B43 V7; http://disc.gsfc.nasa.gov/datacollection/TRMM_3B43_V7.shtml), the Hadley Centre Sea Ice and Sea Surface Temperature data set (HadISST; <http://www.metofice.gov.uk/hadobs/hadisst>), ECMWF (ERA Interim reanalysis; <http://apps.ecmwf.int/datasets>), Atmospheric Infrared Sounder project at Jet Propulsion Laboratory (AIRS; <http://airs.jpl.nasa.gov>). We also acknowledge the World Climate Research Programs (WCRP) Working Group on Coupled Modeling (WGCM), which is responsible for Coupled Model Intercomparison Project (CMIP), and the U.S. Department of Energy's Program for Climate Model Diagnosis and Intercomparison (PCMDI), which provides coordinating support and leads development of software infrastructure in partnership with the Global Organization for Earth System Science Portals. We thank the climate modeling groups around the world listed in Table 2 of this paper for producing and making available their model output. This study was supported by the PPR 068 "Reducción de Vulnerabilidad y Atención de Emergencias por Desastres" and the project "Impacts of Climate Variability and Climate Change on the Mangrove Ecosystem in Tumbes, Peru" (IDRC 106714).

References

- Adler RF et al (2003) The version 2 Global Precipitation Climatology Project (GPCP) monthly precipitation analysis (1979–present). *J Hydrometeorol* 4:1147–1167
- Ashfaq M, Skinner C, Diffenbaugh N (2011) Influence of SST biases on future climate change projections. *Clim Dyn* 36(7–8):1303–1319. doi:[10.1007/s00382-010-0875-2](https://doi.org/10.1007/s00382-010-0875-2)
- Back LE, Bretherton CS (2009a) On the relationship between SST gradients, boundary layer winds, and convergence over the tropical oceans. *J Clim* 22:4182–4196
- Back LE, Bretherton CS (2009b) A simple model of climatological rainfall and vertical motion patterns over the tropical oceans. *J Clim* 22:6477–6497
- Bellucci A, Gualdi S, Navarra A (2010) The double-ITCZ syndrome in coupled general circulation models: the role of large-scale vertical circulation regimes. *J Clim* 23(5):1127–1145
- Belmadani A, Echevin V, Codron F, Takahashi K, Junquas C (2013) What dynamics drive future wind scenarios for coastal upwelling off Peru and Chile? *Clim Dyn* 43:1893. doi:[10.1007/s00382-013-2015-2](https://doi.org/10.1007/s00382-013-2015-2)
- Betts AK, Ridgway W (1989) Climatic equilibrium of the atmospheric convective boundary layer over a tropical ocean. *J Atmos Sci* 46:2621–2641
- Bhat GS, Srinivasan J, Gadgil S (1996) Tropical deep convection, convective available potential energy and sea surface temperature. *J Meteor Soc Jpn* 74:155–166
- Biasutti M, Sobel A, Kushnir Y (2006) AGCM precipitation biases in the Tropical Atlantic. *J Clim* 19:935–957
- Bjerknes J (1969) Atmospheric teleconnections from the equatorial Pacific. *Mon Wea Rev* 97:163–172
- Bony S, Bellon G, Klocke D, Sherwood S, Fermepin S, Denvil S (2013) Robust direct effect of carbon dioxide on tropical circulation and regional precipitation. *Nat Geosci* 6:447–451
- Bretherton CS, Widmann M, Dymnikov VP, Wallace JM, Blad I (1999) The effective number of spatial degrees of freedom of a time-varying field. *J Clim* 12(7):1990–2009
- Brown JR, Power SB, Delage FP, Colman RA, Moise AF, Murphy BF (2011) Evaluation of the south pacific convergence zone in IPCC AR4 climate model simulations of the twentieth century. *J Clim* 24(6):1565–1582. doi:[10.1175/2010JCLI3942.1](https://doi.org/10.1175/2010JCLI3942.1)
- Brown JR, Moise AF, Colman RA (2013) The south pacific convergence zone in CMIP5 simulations of historical and future climate. *Clim Dyn* 41:2179–2197. doi:[10.1007/s00382-012-1591-x](https://doi.org/10.1007/s00382-012-1591-x)
- Brown J, Matear R, Brown J, Katzfey J (2015) Precipitation projections in the tropical Pacific are sensitive to different types of SST bias adjustment. *Geophys Res Lett*. doi:[10.1002/2015GL066184](https://doi.org/10.1002/2015GL066184)
- Cai W, Borlace S, Lengaigne M, Pv Rensch, Collins M, Vecchi GA, Timmermann A, Santoso A, McPhaden MJ, Wu L, England M, Wang G, Guilyardi E, Jin FF (2014) Increasing frequency of extreme El Niño events due to greenhouse warming. *Nat Clim Change*. doi:[10.1038/nclimate2100](https://doi.org/10.1038/nclimate2100)
- Chadwick RI, Boutle Martin G (2013) Spatial patterns of precipitation change in CMIP5: why the rich do not get richer in the tropics. *J Clim* 26:3803–3822
- Chadwick RI (2016) Which aspects of CO₂ forcing and SST warming cause most uncertainty in projections of tropical rainfall change over land and ocean? *J Clim* 29(7):2493–2509. doi:[10.1175/JCLI-D-15-0777.1](https://doi.org/10.1175/JCLI-D-15-0777.1)
- Chou C, Neelin JD (1999) Cirrus-detrainment temperature feedback. *Geophys Res Lett* 26:1295–1298
- Chou C, Chen C, Tu J (2009) Evaluating the “rich-get-richer” mechanism in tropical precipitation change under global warming. *J Clim* 22:1982–2005
- Chung CTY, Power SB, Arblaster JM, Rashid HA, Roff GL (2014) Nonlinear precipitation response to El Niño and global warming in the Indo-Pacific. *Clim Dyn* 42:1837–1856
- Cornejo-Garrido AG, Stone PH (1977) On the heat balance of the Walker circulation. *J Atmos Sci* 34:1155–1162
- Collins M (2005) El Niño or La Niña-like climate change? *Clim Dyn* 24:89–104
- Collins M, Knutti R, Arblaster J et al (2013) Long-term climate change: projections, commitments and irreversibility. *Climate Change 2013: The Physical Science Basis*, Working Group I
- Dai A (2006) Precipitation characteristics in eighteen coupled climate models. *J Clim* 19:4605–4630
- Davey MK et al (2002) STOIC: a study of coupled model climatology and variability in tropical ocean regions. *Clim Dyn* 18:403–420
- Dee DP et al (2011) The ERA-Interim reanalysis: configuration and performance of the data assimilation system. *Q J R Meteorol Soc* 137(656):553–597
- de Szoeke SP, Xie SP (2008) The tropical eastern Pacific seasonal cycle: assessment of errors and mechanisms in IPCC AR4 coupled ocean-atmosphere general circulation models. *J Clim* 21:2573–2590
- Dewitte B, Takahashi K (2016) Diversity of moderate El Niño events evolution: role of air-sea interactions in the eastern tropical Pacific. Submitted to *Clim Dyn*
- DiNezio PA, Vecchi GA, Soden B, Kirtman BP (2009) Climate response of the Equatorial Pacific to global warming. *J Clim* 22:4873–4892
- Efron B, Tibshirani R (1993) An introduction to the bootstrap. Chapman and Hall, p 436
- Friedman AR, Hwang YT, Chiang JCH, Frierson DMW (2013) Inter-hemispheric temperature asymmetry over the Twentieth Century and in future projections. *J Clim* 26:5419–5433
- Fu RA, Del Genio D, Rossow W (1990) Behavior of deep convective clouds in the tropical Pacific deduced from ISCCP radiance. *J Clim* 3:1129–1152
- Fu RA, Del Genio D, Rossow W (1994) Influence of ocean surface conditions on atmospheric vertical thermodynamic structure and deep convection. *J Clim* 7:1092–1108
- Gadgil S, Pv Joseph, Joshi NV (1984) Ocean-atmosphere coupling over monsoon regions. *Nature* 312:141–143
- Graham N, Barnett TP (1987) Observations of sea surface temperature and convection over tropical oceans. *Science* 238:657–659

- Grose MR et al (2014) Assessment of the CMIP5 global climate model simulations of the western tropical Pacific climate system and comparison to CMIP3. *Int J Climatol* 34:3382–3399
- Gu G, Zhang C (2001) A spectrum analysis of synoptic-scale disturbances in the ITCZ. *J Clim* 14:2725–2739
- Held IM, Soden BJ (2000) Water vapor feedback and global warming. *Annu Rev Energy Environ* 25:441–475
- Held IM, Soden BJ (2006) Robust responses of the hydrological cycle to global warming. *J Clim* 19:5686–5699
- Holland GJ, Keenan TD (1980) Diurnal variations of convection over the maritime continent. *Mon Wea Rev* 108:223–225
- Huaman L, Takahashi K (2016) The vertical structure of the eastern Pacific ITCZs and associated circulation using the TRMM Precipitation Radar and in situ data. *Geophys Res Lett.* doi:[10.1002/2016GL068835](https://doi.org/10.1002/2016GL068835)
- Huffman GJ et al (1997) The global precipitation climatology project (GPCP) combined precipitation data set. *Bull Am Meteor Soc* 78:5–20
- Huffman GJ, Bolvin DT (2011) Real-time TRMM multi-satellite precipitation analysis data set documentation. NASA/GSFC Laboratory for Atmospheres, p 43. ftp://meso.gsfc.nasa.gov/pub/trmmdocs/rt/3B4XRT_doc_V7.pdf
- Huang P, Xie SP, Hu K, Huang G, Huang R (2013) Patterns of the seasonal response of tropical rainfall to global warming. *Nat Geosci* 6:357–361
- Huang P (2014) Regional response of annual-mean tropical rainfall to global warming. *Atmos Sci Lett* 15:103–109
- Hurrell J, Hack J, Shea D, Caron J, Rosinski J (2008) A new sea surface temperature and sea ice boundary dataset for the community atmosphere model. *J Clim* 21:5145–5153. doi:[10.1175/2008JCLI2292.1](https://doi.org/10.1175/2008JCLI2292.1)
- IPCC (2005) Guidance notes for lead authors of the IPCC fourth assessment report on addressing uncertainties
- Johnson NC, Xie SP (2010) Changes in the sea surface temperature threshold for tropical convection. *Nat Geosci* 3:842–845
- Johnson NC, Kosaka Y (2016) The impact of eastern equatorial Pacific convection on the diversity of boreal winter El Niño teleconnection patterns. *Clim Dyn.* doi:[10.1007/s00382-016-3039-1](https://doi.org/10.1007/s00382-016-3039-1)
- Kanamitsu M, Ebisuzaki W, Woollen J, Yang SK, Hnilo JJ, Fiorino M, Potter GL (2002) NCEP-DOE AMIP-II reanalysis (R-2). *Bull Am Meteor Soc* 83:1631–1643
- Kharin VV, Zwiers FW, Zhang X, Wehner M (2013) Changes in temperature and precipitation extremes in the CMIP5 ensemble. *Clim Change*. doi:[10.1007/s10584-013-0705-8](https://doi.org/10.1007/s10584-013-0705-8)
- Kent C, Chadwick R, Rowell DP (2015) Understanding uncertainties in future projections of seasonal tropical precipitation. *J Clim* 28:4390–4413
- Kleeman R (1991) A simple model of the atmospheric response to ENSO sea surface temperature anomalies. *J Atmos Sci* 48:3–18
- Kummerow C et al (2000) The status of the tropical rainfall measuring mission (TRMM) after two years in orbit. *J Appl Meteor* 39:1965–1982
- Larson K, Hartmann DL, Klein SA (1999) The role of clouds, water vapor, circulation, and boundary layer structure in the sensitivity of the tropical climate. *J Clim* 12:2359–2374
- Lau KM, Shen S (1988) On the dynamics of intraseasonal oscillations and ENSO. *J Atmos Sci* 45:1781–1797
- Lau K-M, Wu HT, Bony S (1997) The role of large-scale atmospheric circulation in the relationship between tropical convection and sea surface temperature. *J Clim* 10:381–392
- Li G, Xie SP (2014) Tropical biases in CMIP5 multi-model ensemble: the excessive equatorial Pacific cold tongue and double ITCZ problems. *J Clim.* doi:[10.1175/jcli-d-13-00337.1](https://doi.org/10.1175/jcli-d-13-00337.1)
- Lin JL (2007) The double-ITCZ problem in IPCC AR4 coupled GCMs: oceanatmosphere feedback analysis. *J Clim* 20:4497–4525
- Lintner BR, Neelin JD (2008) Eastern margin variability of the South Pacific Convergence Zone. *Geophys Res Lett.* doi:[10.1029/2008GL034298](https://doi.org/10.1029/2008GL034298)
- Li B, Zhou T (2011) ENSO-related principal interannual variability modes of early and late summer rainfall over East Asia in SST-driven AGCM simulations. *J Geophys Res.* doi:[10.1029/2011JD015691](https://doi.org/10.1029/2011JD015691)
- Liu Z, Vavrus S, He F, Wen N, Zhong Y (2005) Rethinking tropical ocean response to global warming: the enhanced equatorial warming. *J Clim* 18:4684–4700
- Lu J, Zhao B (2012) The role of oceanic feedback in the climate response to doubling CO₂. *J Clim* 25:7544–7563
- Ma J, Xie SP (2013) Regional patterns of sea surface temperature change: a source of uncertainty in future projections of precipitation and atmospheric circulation. *J Clim* 26:2482–2501
- Manabe S, Hahn DG, Holloway JL (1974) The seasonal variation of the tropical circulation as simulated by a global model of the atmosphere. *J Atmos Sci* 31:43–83
- Mapes BE (1997) Equilibrium vs. activation controls on large-scale variations of tropical deep convection. In: Smith RK (ed) The physics and parameterization of moist atmospheric convection. Kluwer Acad, pp 321–358
- Masson D, Knutti R (2011) Climate model genealogy. *Geophys Res Lett.* doi:[10.1029/2011GL046864](https://doi.org/10.1029/2011GL046864)
- Mechoso CR et al (1995) The seasonal cycle over the tropical Pacific in coupled oceanatmosphere general circulation models. *Mon Wea Rev* 123:2825–2838
- Meehl GA, Washington WM (1996) El Niño-like climate change in a model with increased atmospheric CO₂ concentrations. *Nature* 382:56–60
- Meehl GA, Covey C, McAvaney B, Latif M, Stouffer RJ (2005) Overview of the coupled model intercomparison project. *Bull Am Meteor Soc* 86:89–93
- Meenu S, Parameswaran K, Rajeev K (2012) Role of sea surface temperature and wind convergence in regulating convection over the tropical Indian Ocean. *J Geophys Res.* doi:[10.1029/2011JD016947](https://doi.org/10.1029/2011JD016947)
- Miller RL (1997) Tropical thermostats and low cloud cover. *J Clim* 10:409–440
- Neale R, Slingo J (2003) The maritime continent and its role in the global climate: a GCM study. *J Clim* 16:834–848
- Neelin JD, Held IM (1987) Modeling tropical convergence based on the moist static energy budget. *Mon Wea Rev* 115:3–12
- Neelin JD, Chou C, Su H (2003) Tropical drought regions in global warming and El Niño teleconnections. *Geophys Res Lett.* doi:[10.1029/2003GL018625](https://doi.org/10.1029/2003GL018625)
- Newell RE (1979) Climate and the ocean. *Am Sci* 67:405–416
- Oueslati B, Bellon G (2015) The double ITCZ bias in CMIP5 models: interaction between SST, large-scale circulation and precipitation. *Clim Dyn* 44:585–607. doi:[10.1007/s00382-015-2468-6](https://doi.org/10.1007/s00382-015-2468-6)
- Parsons DB, Yoneyama K, Redelsperger JL (2000) The evolution of the tropical western Pacific atmosphere-ocean system following the arrival of a dry intrusion. *Q J Roy Meteor Soc* 126:517–548
- Pierrehumbert R (1995) Thermostats, radiator fins, and the run-away greenhouse. *J Atmos Sci* 52:1784–1806
- Power S, Delage F, Chung C, Kociuba G, Keay K (2013) Robust twenty-first-century projections of El Niño and related precipitation variability. *Nature*. doi:[10.1038/nature12580](https://doi.org/10.1038/nature12580)
- Rajendran K, Nanjundiah RS, Gadgil S, Srinivasan J (2012) How good are the simulations of tropical SST-rainfall relationship by IPCC AR4 atmospheric and coupled models? *J Earth Syst Sci.* doi:[10.1007/s12040-012-0185-7](https://doi.org/10.1007/s12040-012-0185-7)
- Ramanathan V, Collins W (1991) Thermodynamic regulation of ocean warming by cirrus clouds deduced from observations of the 1987 El Niño. *Nature* 351:27–32

- Raymond DJ, Raga GB, Bretherton CS, Molinari J, López-Carrillo C, Fuchs Ž (2003) Convective forcing in the intertropical convergence zone of the eastern Pacific. *J Atmos Sci* 60:2064–2082
- Rayner NA, Parker DE, Horton EB, Folland CK, Alexander LV, Rowell DP, Kent EC, Kaplan A (2003) Global analyses of sea surface temperature, sea ice, and night marine air temperature since the late nineteenth century. *J Geophys Res* 108(D14):4407. doi:[10.1029/2002JD002670](https://doi.org/10.1029/2002JD002670)
- Reynolds RW, Rayner NA, Smith TM, Stokes DC, Wang W (2002) An improved in situ and satellite SST analysis for climate. *J Clim* 15:1609–1625
- Reynolds RW, Smith TM (1994) Improved global sea surface temperature analyses using optimum interpolation. *J Clim* 7:929–948
- Richter I, Xie SP, Behera SK, Doi T, Masumoto Y (2014) Equatorial Atlantic variability and its relation to mean state biases in CMIP5. *Clim Dyn* 42(12):171–188
- Saito K, Keenan T, Holland G, Puri K (2001) Numerical simulation of the diurnal evolution of tropical convection over the Maritime Continent. *Mon Wea Rev* 129:378–400
- Seager R, Murtugudde R (1997) Ocean dynamics, thermocline adjustment, and regulation of tropical SST. *J Clim* 10:521–534
- Siongco AC, Hohenegger C, Stevens B (2014) The Atlantic ITCZ bias in CMIP5 models. *Clim Dyn* 45:1169–1180
- Sobel AH, Gildor H (2003) A simple time-dependent model of SST hot spots. *J Clim* 16:3978–3992
- Sobel A, Camargo S (2011) Projected future seasonal changes in tropical summer climate. *J Clim* 24:473–487. doi:[10.1175/2010JCLI3748.1](https://doi.org/10.1175/2010JCLI3748.1)
- Song XL, Zhang GJ (2014) Role of climate feedback in El Niño-like SST response to global warming. *J Clim* 27:7301–7318
- Stockdale T, Balmaseda M, Vidard A (2006) Tropical Atlantic SST prediction with coupled oceanatmosphere GCMs. *J Clim* 19:6047–6061
- Sud Y, Walker G, Lau K (1999) Mechanisms regulating sea surface temperatures and deep convection in the tropics. *Geophys Res Lett* 26:1019–1022
- Susskind J, Blaisdell M, Iredell L, Keita F (2011) Improved temperature sounding and quality controlmethodology using AIRS/AMSU data: the AIRS Science Team version 5 retrieval algorithm. *IEEE Trans Geosci Remote Sens* 49:883–907
- Takahashi K (2009a) Radiative constraints on the hydrological cycle in an idealized radiativeconvective equilibrium model. *J Atmos Sci.* doi:[10.1175/2008JAS2797.1](https://doi.org/10.1175/2008JAS2797.1)
- Takahashi K (2009b) The global hydrological cycle and atmospheric shortwave absorption in climate models under CO₂ forcing. *J Clim.* doi:[10.1175/2009JCLI2674.1](https://doi.org/10.1175/2009JCLI2674.1)
- Takahashi K, Battisti DS (2007a) Processes controlling the mean tropical Pacific precipitation pattern. Part I: The Andes and the eastern Pacific ITCZ. *J Clim* 20:3434–3451
- Takahashi K, Battisti DS (2007b) Processes controlling the mean tropical Pacific precipitation pattern. Part II: The SPCZ and the southeast Pacific dry zone. *J Clim* 20:5696–5706
- Takahashi K, Dewitte B (2016) Strong and moderate nonlinear El Niño regimes. *Clim Dyn.* doi:[10.1007/s00382-015-2665-3](https://doi.org/10.1007/s00382-015-2665-3)
- Taylor K, Stouffer R, Meehl G (2012) An overview of CMIP5 and the experiment design. *Bull Am Meteor Soc* 93:485–498. doi:[10.1175/BAMS-D-11-00094.1](https://doi.org/10.1175/BAMS-D-11-00094.1)
- Tian B, Fetzer E, Kahn B, Teixeira J, Manning E, Hearty T (2013) Evaluating CMIP5 models using AIRS tropospheric air temperature and specific humidity climatology. *J Geophys Res.* doi:[10.1029/2012JD018607](https://doi.org/10.1029/2012JD018607). http://disc.sci.gsfc.nasa.gov/AIRS/documentation/v6_docs/v6releasedocs-1/V6_L3_User_Guide.pdf
- Tompkins A (2001) On the relationship between tropical convection and sea surface temperature. *J Clim* 14:633–637. doi:[10.1175/1520-0442\(2001\)014<0633:OTRBTC>2.0.CO;2](https://doi.org/10.1175/1520-0442(2001)014<0633:OTRBTC>2.0.CO;2)
- Vecchi G, Soden B (2007a) Global warming and the weakening of the tropical circulation. *J Clim* 20:4316–4340
- Vecchi G, Soden B (2007b) Effect of remote sea surface temperature change on tropical cyclone potential intensity. *Nature* 450(7172):1066–1070
- Waliser DE, Graham NE, Gautier C (1993) Comparison of the highly reflective cloud and outgoing long-wave radiation datasets for use in estimating tropical deep convection. *J Clim* 6:331–353
- Waliser DE, Graham NE (1993) Convective cloud systems and warm-pool surface temperatures: coupled interactions and self-regulation. *J Geophys Res* 98:12881–12893
- Waliser DE, Somerville RJC (1994) Preferred latitudes of the intertropical convergence zone. *J Atmos Sci* 51:1619–1639
- Wallace JM (1992) Effect of deep convection on the regulation of tropical sea surface temperature. *Nature* 357:230–231
- Wang B, Liu J, Yang J, Zhou T, Wu Z (2009) Distinct principal modes of early and late summer rainfall anomalies in East Asia. *J Clim* 22:3864–3875
- Wang B, Li T (1993) A simple tropical atmosphere model of relevance to short-term climate variations. *J Atmos Sci* 50:260–284
- Widlansky M, Webster P, Hoyos C (2010) On the location and orientation of the South Pacific Convergence Zone. *Clim Dyn.* doi:[10.1007/s00382-010-0871-6](https://doi.org/10.1007/s00382-010-0871-6)
- Williams M, Houze R (1987) Satellite-observed characteristics of winter monsoon cloud clusters. *Mon Wea Rev* 115:505–519
- Williams E, Renno N (1993) An analysis of the conditional instability of the tropical atmosphere. *Mon Weather Rev* 121:21–36. doi:[10.1175/1520-0493\(1993\)121<0021:AAOTCI>2.0.CO;2](https://doi.org/10.1175/1520-0493(1993)121<0021:AAOTCI>2.0.CO;2)
- Xie S, Philander S (1994) A coupled ocean-atmosphere model of relevance to the ITCZ in the eastern Pacific. *Tellus* 46A:340–350
- Xie P, Arkin PA (1997) Global precipitation: a 17-year monthly analysis based on gauge observations, satellite estimates, and numerical model outputs. *Bull Am Meteor Soc* 78:2539–2558
- Xie S (2004) The shape of continents, air-sea interaction, and the rising eastern Pacific. In: Henry FD, Raymond SB (Eds) The Hadley circulation: present, past and future, vol 21 of the series Advances in Global Change Research, pp 121–152
- Xie S, Deser C, Vecchi G, Ma J, Teng H, Wittenberg A (2010) Global warming pattern formation: sea surface temperature and rainfall. *J Clim* 23:966–986. doi:[10.1175/2009JCLI3329.1](https://doi.org/10.1175/2009JCLI3329.1)
- Yang G, Slingo JM (2001) The diurnal cycle in the tropics. *Mon Wea Rev* 129:784–801
- Yin X, Gruber A, Arkin P (2004) Comparison of the GPCP and CMAP merged gaugesatellite monthly precipitation products for the period 1979–2001. *J Hydrometeorol* 5(6):1207–1222
- Ying J, Huang P, Huang R (2015) Evaluating the formation mechanisms of the equatorial Pacific SST warming pattern in CMIP5 models. *Adv Atmos Sci* 33:433–441. doi:[10.1007/s00376-015-5184-6](https://doi.org/10.1007/s00376-015-5184-6)
- Yu JY, Mechoso CR (1999) Links between annual variations of Peruvian stratocumulus clouds and of SST in the eastern equatorial Pacific. *J Clim* 12:3305–3318
- Zeng N, Neelin JD (1999) A land–atmosphere interaction theory for the tropical deforestation problem. *J Clim* 12:857–872
- Zhang C (1993) Large-scale variability of atmospheric deep convection in relation to sea surface temperature in the tropics. *J Clim* 6:1898–1913
- Zhang C (2001) Double ITCZs. *J Geophys Res.* doi:[10.1029/2000JD900046](https://doi.org/10.1029/2000JD900046)
- Zhang L, Li T (2014) A simple analytical model for understanding the formation of Sea surface temperature patterns under global warming. *J Clim* 27:8413–8421
- Zhang X, Liu H, Zhang M (2015) Double ITCZ in coupled ocean-atmosphere models: From CMIP3 to CMIP5. *Geophys Res Lett.* doi:[10.1002/2015GL065973](https://doi.org/10.1002/2015GL065973)